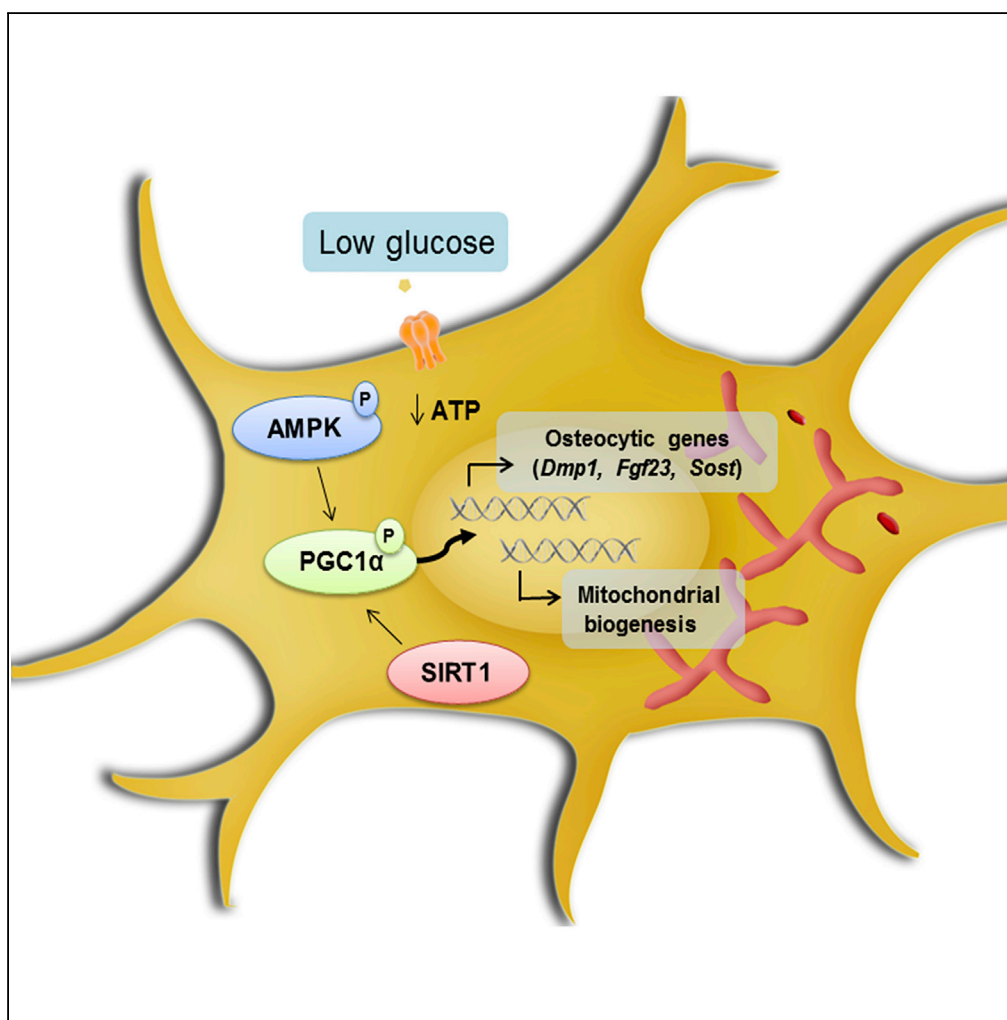**Article**

Glucose Restriction Promotes Osteocyte Specification by Activating a PGC-1α-Dependent Transcriptional Program

Cristina Sánchez-de-Diego, Natalia Artigas, Carolina Pimenta-Lopes, ..., Pablo M. Garcia-Roves, José Luis Rosa, Francesc Ventura

fventura@ub.edu

HIGHLIGHTS

Glucose restriction promotes osteocytic gene expression and mitochondrial function

Glucose restriction triggers activation of the AMPK/PGC-1 pathway

Effects of glucose restriction on osteocyte gene expression depend on *Ppargc1a/b*

Deletion of *Ppargc1a/b* in osteoblasts and osteocytes leads to osteopenia

iScience

Article

Glucose Restriction Promotes Osteocyte Specification by Activating a PGC-1α-Dependent Transcriptional Program

Cristina Sánchez-de-Diego,[1] Natalia Artigas,[1] Carolina Pimenta-Lopes,[1] José Antonio Valer,[1] Benjamin Torrejon,[2] Pau Gama-Pérez,[1] Josep A. Villena,[3] Pablo M. Garcia-Roves,[1] José Luis Rosa,[1] and Francesc Ventura[1,4,*]

SUMMARY

Osteocytes, the most abundant of bone cells, differentiate while they remain buried within the bone matrix. This encasement limits their access to nutrients and likely affects their differentiation, a process that remains poorly defined. Here, we show that restriction in glucose supply promotes the osteocyte transcriptional program while also being associated with increased mitochondrial DNA levels. Glucose deprivation triggered the activation of the AMPK/PGC-1 pathway. AMPK and SIRT1 activators or PGC-1α overexpression are sufficient to enhance osteocyte gene expression in IDG-SW3 cells, murine primary osteoblasts, osteocytes, and organotypic/*ex vivo* bone cultures. Conversely, osteoblasts and osteocytes deficient in *Ppargc1a* and *b* were refractory to the effects of glucose restriction. Finally, conditional ablation of both genes in osteoblasts and osteocytes generate osteopenia and reduce osteocytic gene expression in mice. Altogether, we uncovered a role for PGC-1 in the regulation of osteocyte gene expression.

INTRODUCTION

Of the major cell types in bone, osteocytes make up over 90% to 95% of total bone cells in the adult skeleton. No longer considered passive placeholders in bone, osteocytes have recently emerged as major orchestrators of bone remodeling, physical mechanosensors, hematopoietic niche cells, and endocrine regulators of whole-body metabolism (Dallas et al., 2013; Sato et al., 2013; Karsenty and Olson, 2016). Lower osteocyte function has been directly linked to mechanical bone fragility, osteopenia associated with aging or diabetes, chronic kidney disease, and atherosclerosis (Dallas et al., 2013; Lai et al., 2015; Napoli et al., 2017).

Osteocytes derive from osteoblasts through an active and dynamic process involving their embedding in mineralized osteoid matrices. During osteocytogenesis dramatic morphological changes occur, including an important restructuring of the cytoskeleton and acquisition of a unique gene expression profile (Bonewald, 2011). As osteocytogenesis progresses, we see the downregulation of some osteoblastic genes and the progressive expression of osteocyte-specific genes such as *Dmp1*, *Fgf23,* and *Sost* (Woo et al., 2011). Yet the genetic and molecular mechanisms that govern the differentiation and maturation of osteocytes are far from clear.

One of the driving forces of osteoblast-osteocyte transition is likely to be their encasement within a mineralized bone matrix. This restricts their access to oxygen and nutrients and can induce modifications in their metabolic profile (Riddle and Clemens, 2017). The lacuno-canalicular system connects osteocytes between these matrices and allows those near the surface to interact with osteoblasts and bone-lining cells (Buenzli and Sims, 2015). However, the mechanisms of diffusion between the bone surface and the osteocytes are challenged to maintain an adequate supply and exchange of nutrients and metabolic products (Piekarski and Munro, 1977; Petrov and Pollack, 2003; Wang, 2018). Therefore we can infer that osteoblasts, as they differentiate into osteocytes, must adapt to a nutrient-restricted environment. For instance, osteocytes are enriched in proteins involved in hypoxic response, and hypoxic conditions promote the expression of osteocytic genes (Hirao et al., 2007; Guo et al., 2010; Dallas et al., 2013).

It has been shown that osteocytes maintain oxidative status utilizing mainly aerobic mitochondrial pathways (Frikha-Benayed et al., 2016). In contrast, osteoprogenitors and osteoblasts represent by far the

[1]Departament de Ciències Fisiològiques, Universitat de Barcelona, IDIBELL, L'Hospitalet de Llobregat, 08907 Barcelona, Spain

[2]Centres Científics i Tecnològics, Universitat de Barcelona, L'Hospitalet de Llobregat, Barcelona 08907, Spain

[3]Laboratory of Metabolism and Obesity, Vall d'Hebron Institut de Recerca, Universitat Autònoma de Barcelona, Barcelona 08035, Spain

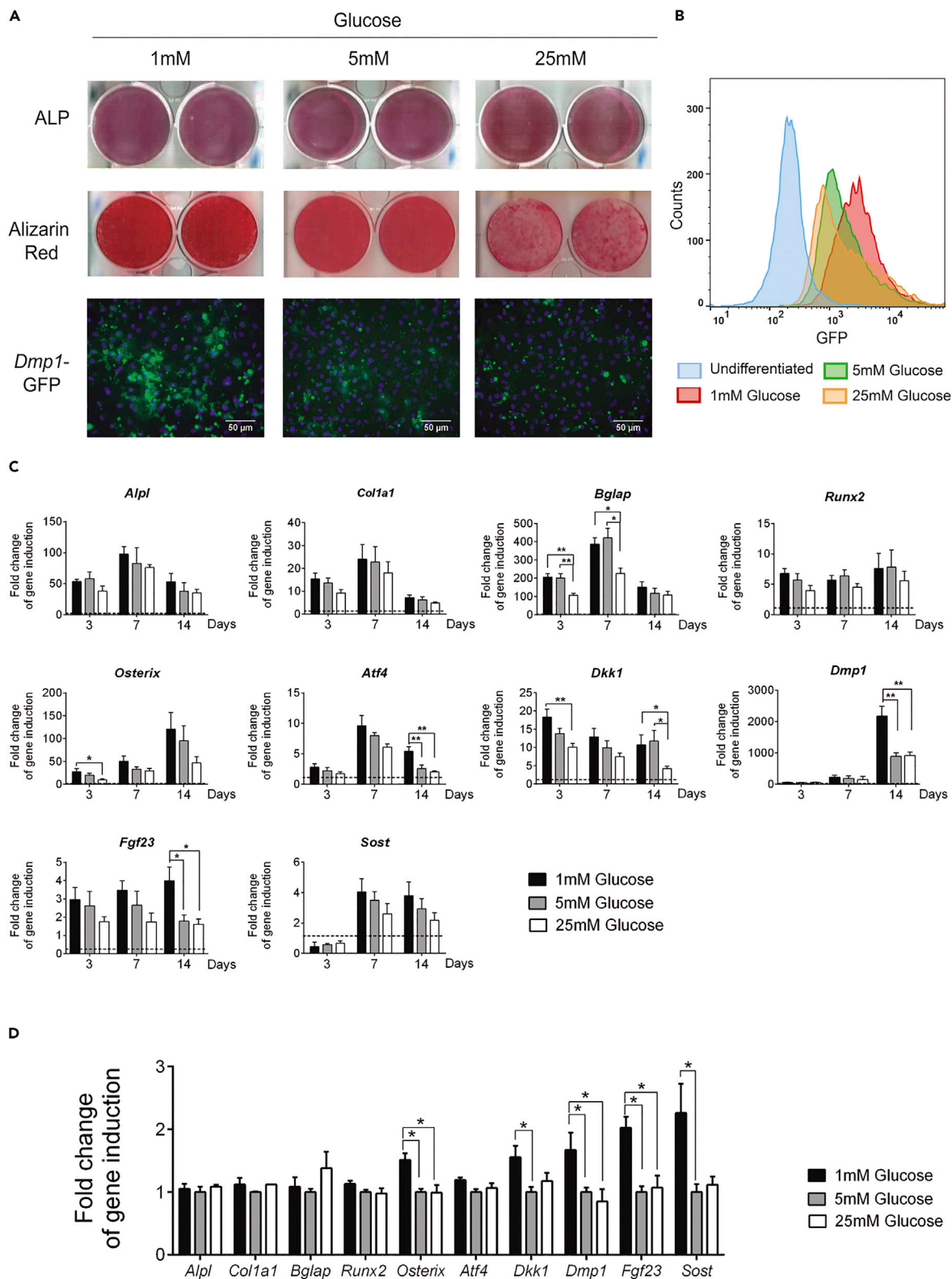[4]Lead Contact

*Correspondence: fventura@ub.edu

Figure 1. Effect of Glucose Supply in Osteocyte Differentiation

(A) Representative images of alkaline phosphatase staining (ALP), alizarin red staining, and visualization of *Dmp1*-GFP expression in IDG-SW3 differentiated for 14 days in the presence of 1, 5, or 25 mM glucose. Cell nuclei were stained with DAPI (blue).

(B) Flow cytometry analysis of *Dmp1*-GFP expression in IDG-SW3 undifferentiated and differentiated cells for 14 days in the presence of 1, 5, or 25 mM glucose.

(C) mRNA expression profile of osteoblast and osteocyte gene markers during IDG-SW3 differentiation (at 3, 7, and 14 days) in the presence of 1, 5, and 25 mM glucose.

(D) Quantification of mRNA expression levels in primary osteocytes cultured for 4 days in the presence of 1, 5, or 25 mM glucose. mRNA levels were measured by qRT-PCR and normalized to *Tbp* expression.

Results are plotted as expression relative to undifferentiated IDG-SW3 or osteocytes cultured in 5 mM glucose (mean $\pm$ SEM of five to seven independent experiments). *p < 0.05 and **p < 0.01 using one-way ANOVA. See also Figure S1.

most glucose-avid cells in bone with relatively sparse uptake in osteocytes (Dirckx et al., 2018). Glucose is not only used by osteoblasts but also its uptake synergizes with Runx2 to determine bone formation and homeostasis throughout life (Wei et al., 2015). Recent studies have further revealed the importance of aerobic glycolysis for the anabolic effects of parathyroid hormone (PTH) and Wnts (Esen et al., 2013, 2015; Regan et al., 2014). These studies pointed out that modulation of AMPK and/or mTORC1/2 is the mechanism involved in the functional link between glucose metabolism and bone formation.

AMPK acts as a cellular energy sensor and has a critical role in adaptive metabolic reprogramming. Several studies demonstrate that AMPK deletion of AMPKα1, β1, or β2 subunits in mice results in reduced trabecular bone without modifying the numbers of osteoclasts and osteoblasts (Quinn et al., 2010). Once active, AMPK activity leads to higher glucose uptake, autophagy, and mitochondrial biogenesis (Hardie, 2018). Some of these functions are mediated by the proliferator-activated receptor γ co-activator-1 (PGC-1). PGC-1s are transcriptional co-activators that respond to a number of environmental cues and coordinate mitochondrial biogenesis and tissue-specific programs of gene regulation (Villena, 2015). Therefore considering that metabolic rewiring is likely to be crucial for bone cell specification, we hypothesize that low glucose concentration can induce metabolic and genetic reprogramming, which promotes osteocytogenesis.

RESULTS

Glucose Restriction Promotes Osteocyte Differentiation

We investigated the effects of different glucose concentrations, the major source of energy in culture media, on bone cell specification. We differentiated the pre-osteocytic IDG-SW3 cell line and mouse primary osteoblasts in the presence of 1, 5, or 25 mM glucose. Selected glucose concentrations did not affect cell viability or proliferation of IDG-SW3 cells (Figures S1A–S1C). Alkaline phosphatase and alizarin red staining showed the ability of IDG-SW3 cells to differentiate into mature osteoblasts and revealed a decrease in the formation of calcium deposits (alizarin red) when cultured in 25 mM glucose (Figure 1A). Confluent IDG-SW3 cells differentiated into an early stage of osteocyte specification after 14 days in culture at 37°C (Woo et al., 2011). These cells also carry a *Dmp1*-GFP reporter (expression of GFP under the control of the osteocyte-specific *Dmp1* promoter) that facilitates the follow-up of the osteoblast-to-osteocyte transition. Our data showed a negative correlation between osteocytic *Dmp1*-GFP expression and glucose supply. Low glucose supply enhanced the expression of *Dmp1*-GFP, as analyzed by either fluorescence microscopy or fluorescence-activated cell sorting (Figures 1A and 1B). To further characterize the induced phenotype, we quantified mRNAs associated with osteoblasts and osteocytes. Gene expression profiling during the osteoblast-to-osteocyte transition in IDG-SW3 cells indicated that mRNA levels of osteoblastic genes (*Alpl*, *Col1a1*, *Bglap*, or *Atf4*) peaked at the seventh day and decreased thereafter, whereas expression of the osteocytic markers *Dmp1* increased at day 14 (Figure 1C). A high-glucose regime reduced the levels of osteoblast genes, such as *Bglap*, *Osx*, or *Dkk1*. More importantly, glucose restriction (1 mM glucose) significantly increased the expression of the osteocyte markers *Dmp1* and *Fgf23* compared with normoglycemia or hyperglycemia (5 and 25 mM glucose, respectively) (Figure 1C). The effects of distinct glucose concentrations in the osteocytic transcriptional program were independent of changes in the osmotic pressure (Figure S1D). We also investigated the gene expression profile of osteocytes and bone organotypic cultures maintained for 4 and 5 days respectively, with different glucose regimes. As with IDG-SW3 cells, low-glucose media increased the expression of some osteocytic genes (*Dkk1*, *Dmp1*, *Fgf23*, or *Sost*) in osteocytes and bone organotypic cultures (Figures 1D and S1E). Altogether, these data demonstrated that glucose restriction favors osteocytic gene expression.
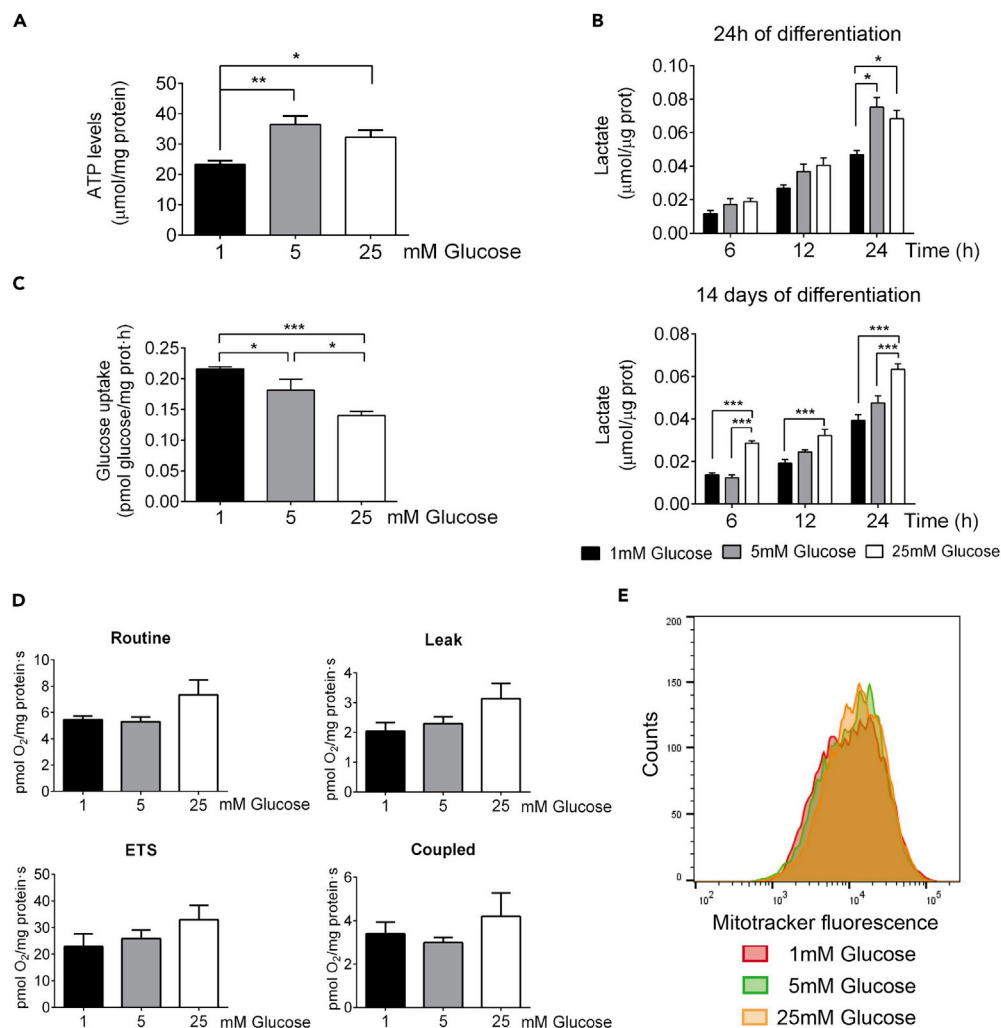
Figure 2. Metabolic Profile Induced by Glucose Supply

(A) ATP levels in IDG-SW3 after 14 days of differentiation in the presence of 1, 5, or 25 mM glucose.

(B) Quantification of lactate release in predifferentiated IDG-SW3 cultured in 1, 5, or 25 mM glucose media for 24 h, and in IDG-SW3 differentiated for 14 days in the presence of 1, 5, or 25 mM glucose.

(C) Determination of the maximal uptake capacity for glucose in IDG-SW3 cells differentiated for 14 days in the presence of 1, 5, or 25 mM glucose.

(D) Determination of routine oxygen consumption, leak respiration (uncoupled), electron transfer capacity (ETS), and coupled respiration of IDG-SW3 differentiated for 14 days in the presence of 1, 5, or 25 mM glucose. A total of 700,000 IDG-SW3 cells were incubated in the respirometry chamber with 1, 5, or 25 mM glucose in α-MEM without FBS during the analysis. All results were expressed relative to protein content. Results are plotted as mean ± SEM of four to eight independent experiments.

(E) Flow cytometry analysis of IDG-SW3 cells differentiated for 14 days in the presence of 1, 5, or 25 mM glucose and labeled with MitoTracker Deep Red.

*$p < 0.05$, **$p < 0.01$, and ***$p < 0.001$ using one-way ANOVA. See also Figure S2.

Glucose Supply Modifies Osteoblast and Osteocyte Metabolism

We then aimed to characterize bone cell metabolism by different glucose concentrations. IDG-SW3 cells differentiated in low-glucose conditions had decreased intracellular ATP levels compared with normogly-cemia or hyperglycemia, which suggests a compromised energy supply (Figure 2A). We assayed lactate released by IDG-SW3 cells during the initial steps of differentiation (24 h) and after complete differentiation (14 days). As expected, either at 24 h or after differentiation, IDG-SW3 cells cultured in low-glucose medium showed a reduction in lactate production, whereas a high-glucose regime raised lactate production values
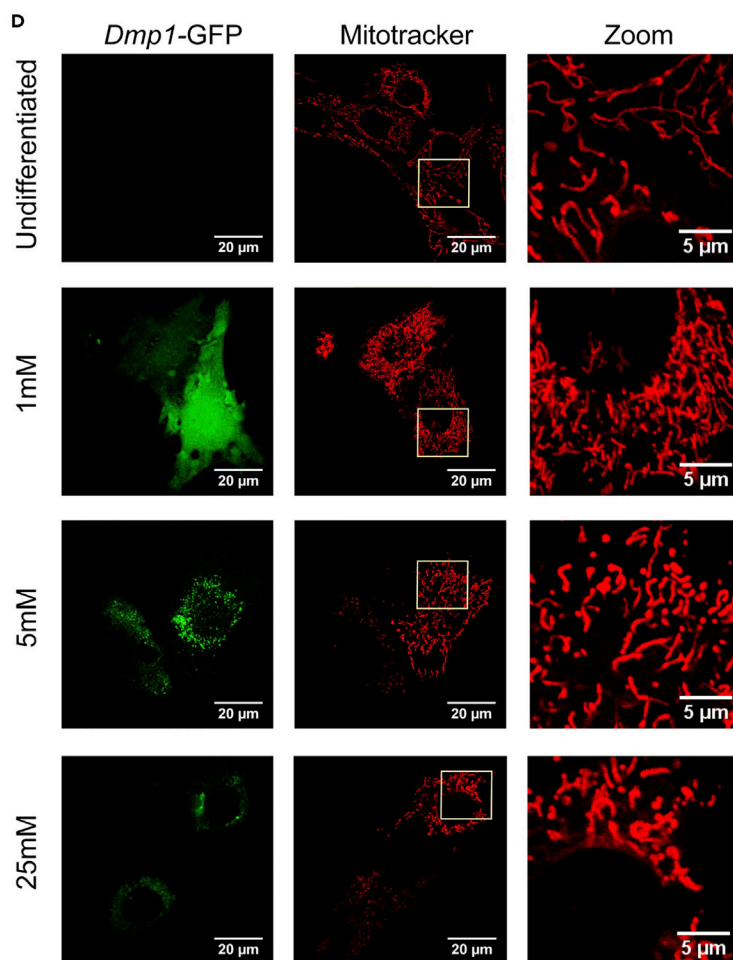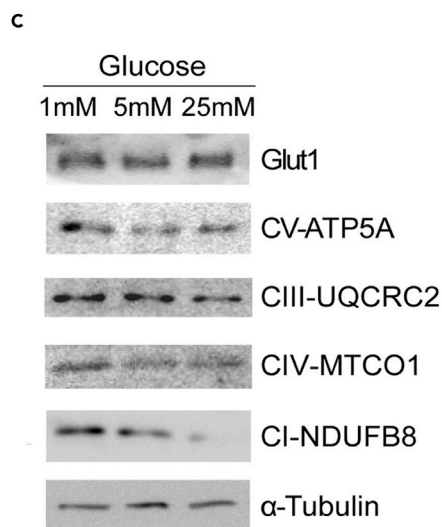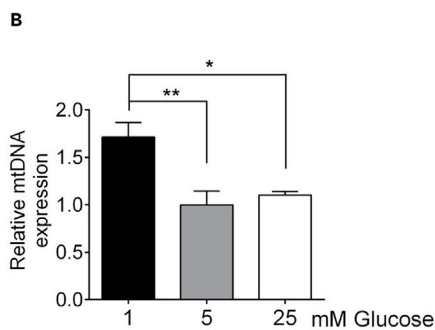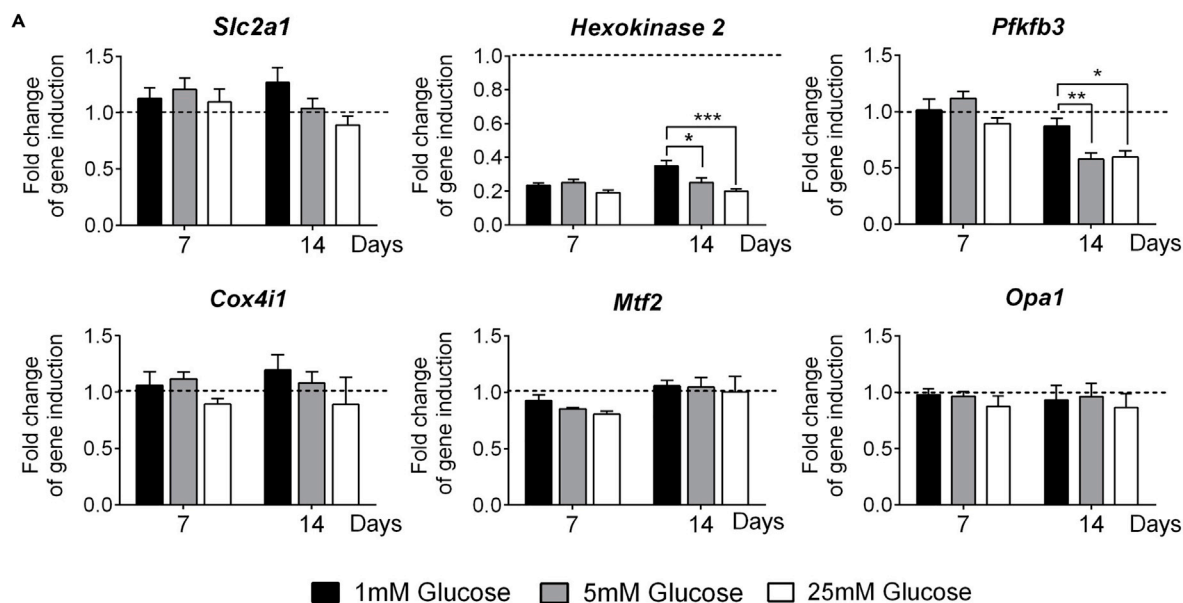
Figure 3. Modification of Glycolytic Gene Expression and Mitochondrial Function Induced by Glucose Supply

(A) mRNA expression levels of glycolytic and mitochondrial genes in IDG-SW3 differentiated for 14 days in the presence of 1, 5, or 25 mM glucose. mRNA expression levels were measured by qRT-PCR and normalized to *Tbp* expression. Results were plotted as expression relative to undifferentiated IDG-SW3 (mean $\pm$ SEM of six independent experiments).

(B) Quantification of mtDNA (*tRNA-Glu*) in IDG-SW3 differentiated for 14 days in the presence of 1, 5, or 25 mM glucose. mtDNA copy number was measured by qPCR and normalized relative to nuclear DNA (*Dmp1* and *Fgf23*). Results are plotted as mean $\pm$ SEM of six independent experiments.

(C) Immunoblot analysis of the expression of Glut1 and mitochondrial complexes in IDG-SW3 differentiated for 14 days in the presence of 1, 5, or 25 mM glucose.

(D) Visualization of mitochondria in IDG-SW3 differentiated for 14 days in the presence of 1, 5, or 25 mM glucose. *Dmp1*-GFP was visualized, and mitochondria were stained with MitoTracker Deep Red.

*$p < 0.05$, **$p < 0.01$, and ***$p < 0.001$ using one-way ANOVA. See also Figure S3.

(Figure 2B). For a further characterization of metabolic reprogramming, we also analyzed glucose uptake capacity after differentiation for 14 days in 1, 5, and 25 mM glucose. Glucose uptake was tested at 10 μM glucose for all conditions. Low glucose exposure significantly increased the uptake capacity for glucose, whereas glucose-enriched media decreased it (Figure 2C). We also investigated the bone cell metabolism in primary osteoblasts cultured for 10 days with different glucose concentrations. Mature primary osteoblasts cultured in 1 mM glucose were still able to maintain ATP levels and, as IDG-SW3 cells, osteoblasts increased their glucose uptake capacity in low-glucose conditions (Figures S2A and S2B). Lactate production was also increased when cultured in 25 mM glucose (Figure S2C). Therefore mature osteoblasts in culture can maintain energetic balance and anaerobic glycolysis even at 1 mM glucose. These data suggested a sparing effect in glucose-restricted conditions, maximizing uptake and reducing lactate release, and vice versa under hyperglycemic conditions.

We then measured mitochondrial respiration in intact, differentiated IDG-SW3 cells using the different glucose supplies. These different glucose concentrations were also maintained during the assay as major energy substrate. We determined routine O_2 consumption, leak state (uncoupled respiration after addition of oligomycin into the assay), electron transfer capacity (determination of electron transfer system [ETS] after carbonylcyanide-4- (trifluoromethoxy)-phenyl-hydrazone (FCCP)), and coupled respiration. Differences in respiratory parameters were not significant between groups, and we only observed a slightly increased routine respiration in cells cultured with 25 mM glucose (Figure 2D). Interestingly, IDG-SW3 cells were able to maintain O_2 consumption under glucose restriction conditions. Moreover, total mitochondrial potential was unmodified by the different glucose regimes when analyzed by flow cytometry using a mitochondrial potential-dependent dye (Figure 2E). It is known that routine respiration is controlled by ATP turnover and substrate availability (Brand and Nicholls, 2011). Therefore these data suggested that cells adapt to meet energy demands by increasing glucose uptake and through the diversion of glucose to mitochondrial respiration.

Glucose Restriction Increases the Mitochondrial DNA and Changes Mitochondrial Morphology

To identify further the changes in energy metabolism induced by glucose supply, we quantified the expression of genes involved in glycolysis and mitochondrial function. GLUT1 (*Slc2a1*) is the most expressed glucose transporter in IDG-SW3 cells during osteocyte specification (Figure S3A). In addition, different glucose concentrations did not induce a significant change in expression between GLUT family members (Figures S3B and 3A). IDG-SW3 cells and osteoblasts differentiated under low-glucose conditions had higher expression of the glycolytic genes *Pfkfb3* and *Hk2*, whereas the expression of *Cox4i1* and the genes involved in mitochondrial fusion/fission *Mtf2* and *Opa1* did not show significant differences between distinct glucose regimes (Figures 3A and S3C). As mitochondria are remarkable dynamic organelles that respond to changes in energy demands, we wondered whether glucose concentration would modify mitochondrial content and function. Reduced glucose supply increased the ratio of mitochondrial DNA (mtDNA) to nuclear DNA (Figures 3B and S3D). This increase in mtDNA was consistent with an increase in the protein levels of members of the different oxidative phosphorylation (OXPHOS) complexes (Figures 3C and S3E).

Emerging evidence showed that mitochondria continuously adjust their shape, size, and network organization through fusion or fission events, to regulate their function (Galloway et al., 2012). Confocal images showed dramatic differences in mitochondrial structure and network among the three conditions. IDG-SW3 cells and primary osteoblasts differentiated in 1 mM glucose media arranged their mitochondria in elongated tubules, with higher branching, forming reticular networks (Figures 3D and S3F). In contrast, hyperglycemic conditions increased mitochondrial fragmentation with the formation of ring-like structures in
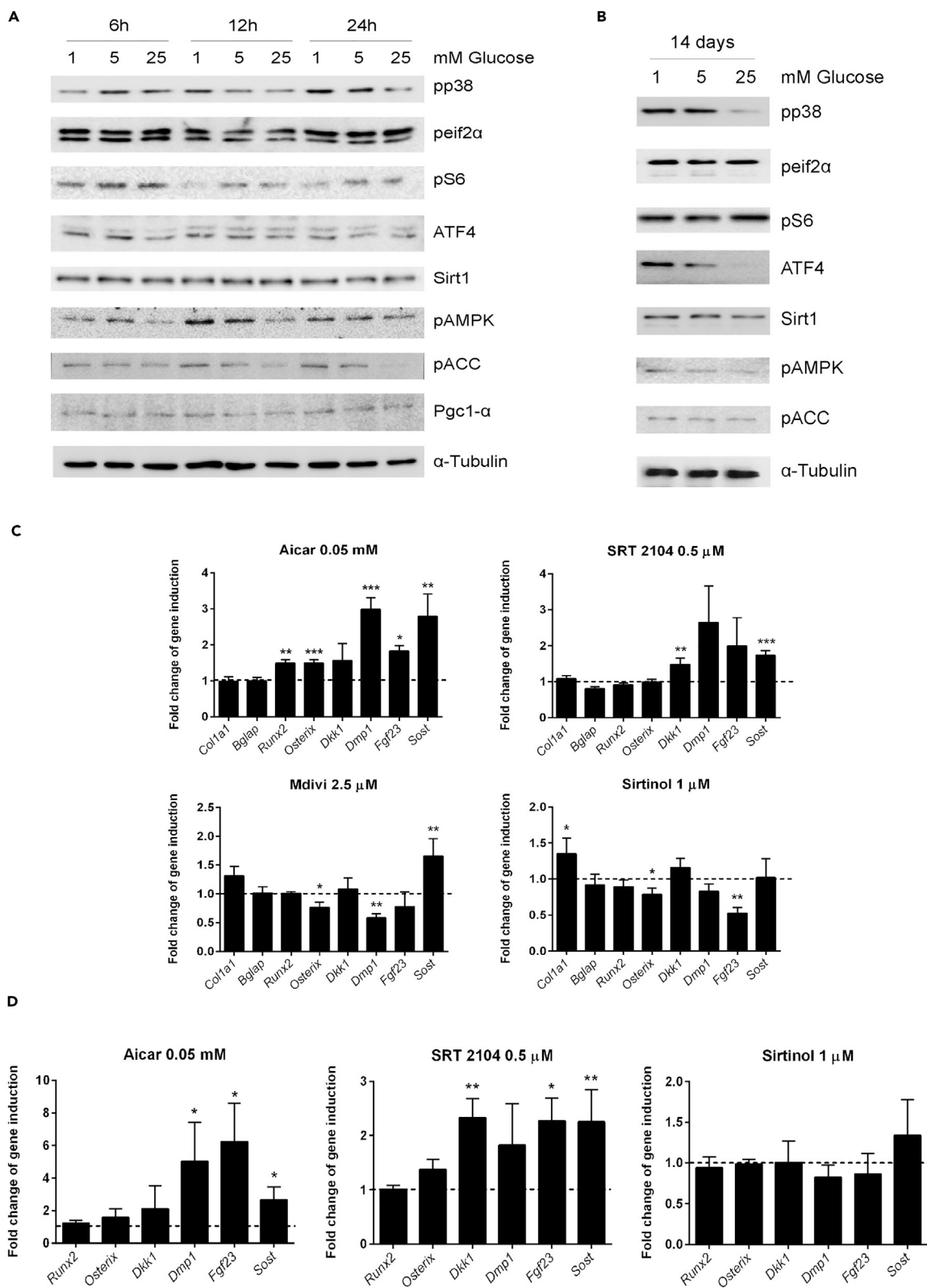
Figure 4. Signaling Pathways Involved in Metabolic and Genetic Reprogramming of Osteocytes

(A and B) Immunoblots from IDG-SW3 cells cultured in 1, 5, and 25 mM glucose media for 6, 12, and 24 h (A) or after 14 days of differentiation in 1, 5, and 25 mM glucose media (B).

(C) mRNA expression of osteoblastic and osteocytic genes in IDG-SW3 differentiated for 14 days in 5 mM glucose and treated with 0.05 mM AICAR (activator of AMPK), 0.5 µM SRT2104 (activator of SIRT1), 1 µM sirtinol (inhibitor of SIRT1), and 2.5 µM Mdivi (inhibitor of mitochondrial fission). mRNA levels were measured by qRT-PCR and normalized to *Tbp* expression. Results were plotted as expression relative to untreated IDG-SW3 (mean ± SEM of five independent experiments).

(D) mRNA expression of osteoblastic and osteocytic genes in organotypic cultures from mouse femur. Organotypic cultures were maintained in 5 mM glucose media and treated with 0.05 mM AICAR, 0.5µM SRT2104, and 1 µM sirtinol for 5 days. mRNA levels were measured by qRT-PCR and normalized to *Tbp* expression.

Results were expressed as gene expression relative to untreated organotypic cultures (mean ± SEM of five independent experiments). *$p < 0.05$, **$p < 0.01$, and ***$p < 0.001$ using Student's t test. See also Figure S4.

differentiated IDG-SW3 and osteoblasts (Figures 3D and S3F). It has been demonstrated that elongated mitochondria are more resistant to mitophagy and more efficient at producing ATP through enhanced cristae density and ATP synthase dimerization (Gomes et al., 2011). In addition, it is known that ring-like and fragmented mitochondria structures arise from cellular stresses (Yu et al., 2006). Therefore these data suggest that during osteocyte differentiation, glucose restriction stimulates glycolytic pathways and increases mtDNA and efficiency in an effort to maintain ATP levels.

Glucose Restriction Effects on Osteocyte Gene Expression Depend on AMPK

Nutrient starvation signals through activation of AMPK and mTORC1 energy sensors (Carroll and Dunlop, 2017). Thus we determined the activation state of signaling pathways likely to be involved in the metabolic and genetic reprogramming of osteocytes. We analyzed early activation of these pathways during the first hours of differentiation and after complete differentiation, in IDG-SW3 and primary osteoblasts. In response to glucose restriction, AMPK and its substrate acetyl-CoA carboxylase (ACC) became phosphorylated (Figures 4A, 4B, S4A, and S4B). Similarly, the stress kinase p38-MAPK was also activated either at 24 h or after 14 days.

Effects of AMPK on mitochondrial biogenesis rely on PGC-1 (PGC1-α and β) expression and activation (Hardie, 2018). The PGC-1 family of transcriptional co-activators plays a major role in integrating physiological signals into the expression of nuclear-encoded mitochondrial genes (Villena, 2015). Posttranslational modifications that activate PGC-1 members include phosphorylation by AMPK and p38 and deacetylation by SIRT1 (Fan et al., 2004; Gerhart-Hines et al., 2007; Jager et al., 2007). Therefore to further characterize the role of AMPK/SIRT/PGC1α/β pathways in osteocyte reprogramming and differentiation, we treated IDG-SW3 cells and bone organotypic cultures with different chemical modulators of these pathways. The activation of AMPK by AICAR during differentiation increased the expression of *Runx2* and *Osx* in IDG-SW3 cells and the expression of *Dmp1*, *Fgf23,* and *Sost* osteocyte genes in both IDG-SW3 and bone organotypic cultures (Figures 4C and 4D). Similarly, the activation of SIRT1 by SRT2104 treatment induced the expression of late osteocyte markers in both experimental models. On the other hand, the inhibition of SIRT1 by sirtinol reduced the levels of *Osx* and *Fgf23* in IDG-SW3 cultures. These results suggested that the activation of AMPK/SIRT1 enhances osteocytic differentiation.

We also evaluated whether induction of mitochondrial fusion and elongation was sufficient for enhancement of osteocytic gene expression. DRP1 is a dynamin-related GTPase that mediates mitochondrial fission (Galloway et al., 2012). Inhibition of DRP1 by Mdivi-1 increases the number of elongated mitochondria and their reticular network (Cassidy-Stone et al., 2008). Inhibition of mitochondrial fission by Mdivi-1 during osteocytic differentiation reduced the expression of *Osx* and *Dmp1* but only induced the expression of *Sost* (Figure 4C). These results suggest that mitochondrial reorganization is not sufficient to enhance osteocytogenesis.

PGC-1 Mediates Enhanced Osteocytic Gene Expression in Response to Reduced Glucose Supply

Next, we determined the expression of *Ppargc1a* and *b* genes during the osteoblast to osteocyte transition in IDG-SW3 cells and primary osteoblasts. Proliferative IDG-SW3 cells expressed higher levels of *Ppargc1a* compared with *Ppargc1b*. Moreover, differentiated cells shifted further toward a major expression of *Ppargc1a* over *Ppargc1b* (Figure 5A). Similarly, the ratio of expression between *Ppargc1a* and *Ppargc1b*
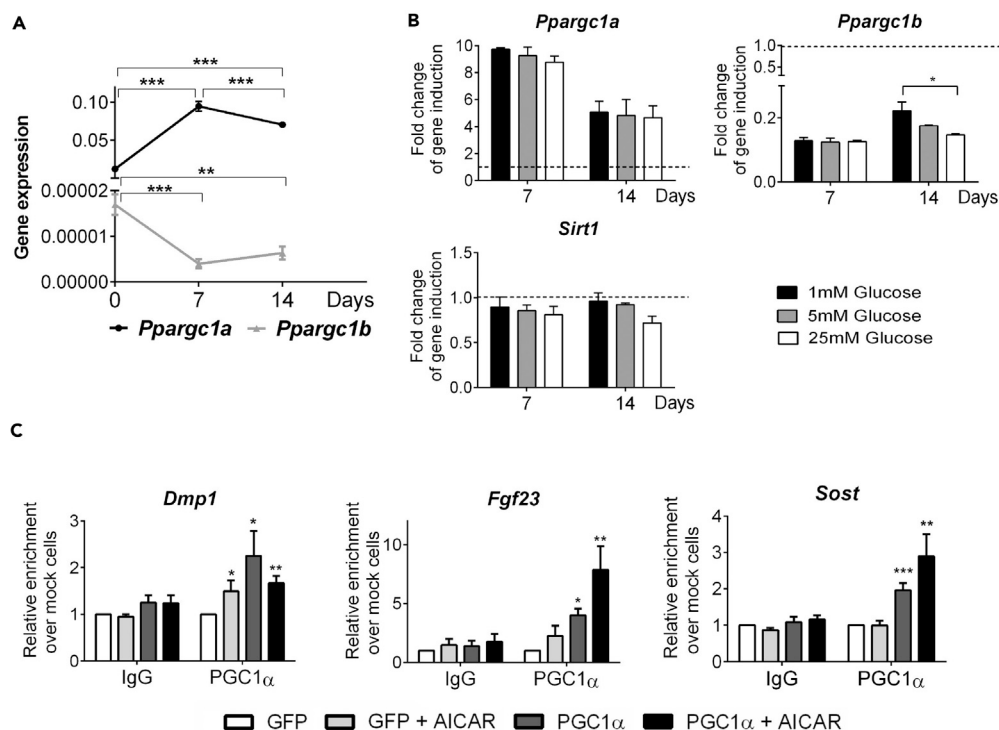
Figure 5. PGC1-α Binds to Osteocytic Promoters

(A) mRNA expression levels of the different isoforms of PGC-1 in IDG-SW3 differentiated for 14 days in 5 mM glucose media. mRNA expression was quantified by qRT-PCR and normalized to *Tbp* expression. Results are plotted as $2^{-\Delta\Delta Ct}$ (mean ± SEM of six independent experiments).

(B) mRNA expression levels of *Ppargc1a*, *Ppargc1b*, and *Sirt1* during IDG-SW3 differentiation in 5 mM glucose media. mRNA levels were quantified by qRT-PCR, normalized by *Tbp* and plotted as expression relative to undifferentiated IDG-SW3 (mean ± SEM of six independent experiments).

(C) Chromatin immunoprecipitation of IDG-SW3 cells infected with control GFP or PGC-1α expression vectors and differentiated in 5 mM glucose media for 5 days in the presence or absence of 0.5 mM AICAR.

Results were normalized to input chromatin and plotted relative to untreated IDG-SW3 cells infected with control GFP vector (mean ± SEM of four independent experiments). *p < 0.05, **p < 0.01, and ***p < 0.001 using Student's t test. See also Figure S4.

in primary osteoblasts and calvarial mRNA was about 3-fold (data not shown). mRNA levels of PGC-1α or SIRT1 did not change among the three culture conditions in IDG-SW3 (Figure 5B). On the contrary, in primary osteoblasts, glucose restriction induced *Ppargc1a* and b mRNA expression (Figure S4C). *Ppargc1a* and *b* play redundant roles by regulating gene expression programs through their interaction with a variety of transcription factors such as NRF2, ERRα, PPARs, or MEF2. *In silico* analysis of regulatory motifs present in the promoters of the osteocyte genes *Dmp1*, *Fgf23*, and *Sost* revealed conserved potential binding sites for PGC-1 co-activated factors. We confirmed the recruitment of PGC-1 to these regulatory regions by chromatin immunoprecipitation with an anti-PGC-1α antibody. Ectopic expression of PGC-1α and its activation with AICAR increased PGC-1α occupancy of *Fgf23* and *Sost* promoters in IDG-SW3 cells (Figure 5C). We also determined whether higher PGC-1α activity could induce expression of these genes. Overexpression of ectopic PGC-1α in IDG-SW3 and primary osteoblasts led to higher mRNA levels of osteoblastic (*Col1a1*, *Bglap*, *Osx*) and osteocytic (*Dkk1*, *Fgf23*, and *Sost*) genes (Figure 6A). We also analyzed gene expression in primary osteoblasts and osteocytes deficient in PGC-1α and PGC-1β. Deletion of *Ppargc1a* and *b* did not affect cell proliferation or viability, although it reduced morphological reorganization and hampered the increase in mtDNA induced by glucose restriction (Figure S5). Deletion of *Ppargc1a* and *Ppargc1b* in primary osteoblasts or osteocytes decreased the levels of *Runx2* and *Osx* irrespective of the glucose regime (Figures 6B and 6C). Furthermore, deletion of *Ppargc1a* and *b* genes abolished the induction of the *Dmp1*, *Fgf23*, and *Sost* mRNAs upon glucose restriction. Altogether, these results proved that PGC-1 co-activators act as regulators of osteocyte gene expression.
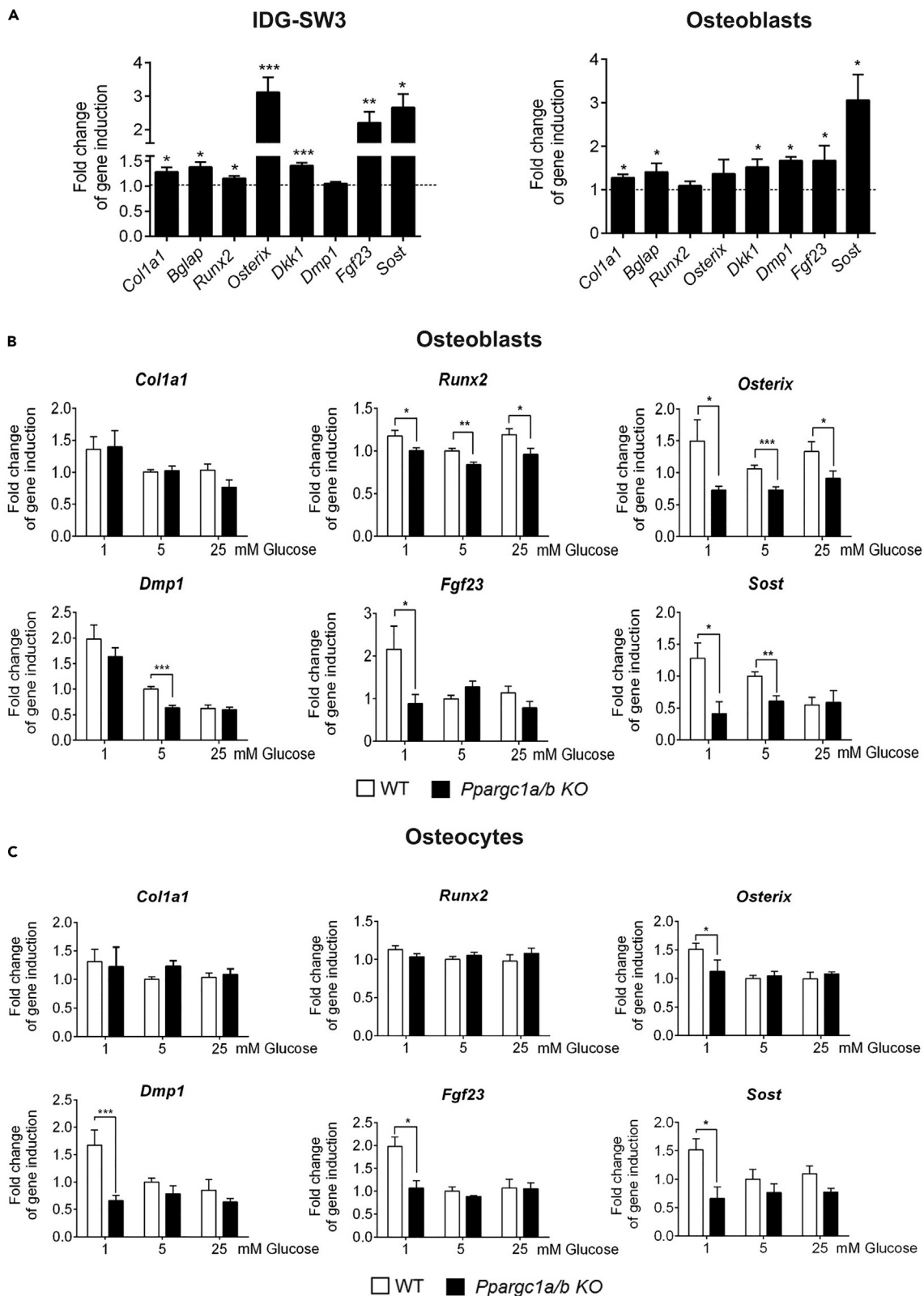
A

IDG-SW3

Osteoblasts

B

Osteoblasts

Col1a1   *Runx2*   *Osterix*

Dmp1   *Fgf23*   *Sost*

☐ WT   ■ *Ppargc1a/b KO*

C

Osteocytes

Col1a1   *Runx2*   *Osterix*

Dmp1   *Fgf23*   *Sost*

☐ WT   ■ *Ppargc1a/b KO*

Figure 6. Role of PGC-1 in Osteocyte Differentiation

(A) mRNA expression levels of IDG-SW3 cells (left) and primary osteoblasts (right) infected with GFP or PGC-1α expression vectors and differentiated in 5 mM glucose media for 5 days. mRNA expression levels were measured by qRT-PCR and normalized to *Tbp* expression. Results were plotted as expression relative to cells infected with GFP vector (mean ± SEM of six to eight independent experiments).

(B and C) mRNA expression levels of osteocytic and osteoblastic genes in primary osteoblasts (B) and primary osteocytes (C) wild-type and knockout for PGC-1α/β. Osteoblasts and osteocytes were isolated from calvarias obtained from *Ppargc1a/b*$^{fl/fl}$ mice and infected with pMSCV-Puro or pMSCV-puro-Cre-ERT2 vectors. Infected cells were cultured for five days in 1, 5, or 25 mM glucose media. mRNA expression levels were measured by qRT-PCR and normalized to *Tbp*. Results are plotted as expression relative to control infection (mean ± SEM of six independent experiments). *p < 0.05, **p < 0.01, and ***p < 0.001 using Student's t test. See also Figures S5 and S6.

Rearrangement of the cytoskeletal organization is a hallmark of osteocytes. In consequence, we examined the arrangement of actin cytoskeleton in IDG-SW3 cells cultured in different glucose concentrations as well as in osteoblasts and osteocytes either wild-type or deficient in *Ppargc1a/b*. We did not find significant differences in any of the conditions (Figure S6).

We further explored the role of *Ppargc1a/b* in bone formation and homeostasis in mice. Transgenic mice for Cre under the control of the 2.3-*Col1a1* promoter (Dacquin et al., 2002) allowed deletion of *Ppargc1a* and *b* in osteoblasts and osteocytes (hereafter *Ppargc1a f/f*; *Ppargc1b f/f*; *Col1a1*-Cre; knockout [KO]) (Figures S7A and S7B). *Ppargc1a/b* deletion did not affect either body weight or femur length. As expected, *Ppargc1a* and *Ppargc1b* mRNA levels in calvaria from KO mice were significantly reduced in both male and female mice (Figures S7C and S7D). We visualized bone formation in male and female mice in distal femurs by micro-computed tomography scanning and histological analysis. In 8 week-old mice, deletion of *Ppargc1a* and *Ppargc1b* led to a decrease in both trabecular and cortical bone architecture. KO male mice presented lower cortical bone volume (BV) associated with reduced cortical thickness, whereas bone perimeter around the midshaft was not affected (Figure 7A). In addition, distal femurs in males also presented less trabecular bone volume (BV/TV) resulting from a significantly lower trabecular number (Tb.N) and trabecular thickness (Tb.Th) (Figure 7A). Trabecular analysis of distal femurs in KO females also showed a significant reduction in BV/TV, Tb.N, and Tb.Th. However, reduction in cortical bone parameters were lower in magnitude and did not reach significant differences (Figure 7B). To clarify the underlying reason for the osteopenic phenotype of the KO mice, we analyzed the expression of osteoblast and osteocyte genes from calvaria. KO male and female mice displayed a reduced expression of osteocyte genes, including *Dmp1*, *Fgf23*, and *Sost*, and increased levels of osteoblastic genes such as *Bglap*, *Runx2*, or *Osx* (Figure 7C). Reduced osteocyte gene expression occurs without significant changes in either the density of osteocytes per bone area or the number of empty lacunae in cortical bone (Figures S8 and S9). Mice deficient for *Ppargc1α/β* showed reduced *Rankl/Opg* ratio of expression in calvaria (Figure S10). Similar results were obtained in osteocytes deficient in *Ppargc1α/β*. These data suggest that although *Ppargc1α/β* affects the expression of *Rankl* and *Opg* in osteocytes, osteopenia in young *Ppargc1α/β*-deficient mice does not arise for increased osteoclastogenesis induced directly by an increased *Rankl/Opg* ratio. In conclusion, our data demonstrate the relevant role of PGC-1 in co-activation of the osteoblast and osteocyte transcriptional programs.

DISCUSSION

In this study, we identified that a reduced supply of glucose facilitates the expression of osteocytic genes in osteoblast/osteocyte precursors. These effects took place in parallel with an increased mtDNA. Glucose reduction triggers the activation of the AMPK/PGC-1 pathway whereas AMPK and SIRT1 activators were sufficient to increase osteocyte gene expression. Osteoblasts and osteocytes deficient in *Ppargc1a* and *b* were refractory for glucose restriction effects, whereas mice deficient in both genes were osteopenic. Our data strongly support modulation of the metabolic state as a strategy for the differentiation of bone cells.

In recent years, several studies have demonstrated that metabolism of osteoblast lineage cells is programmed to optimize energy production to fulfill functional demands throughout their life cycle (Riddle and Clemens, 2017). Early stage of osteoblast specification relies on glycolysis to generate ATP, initiate collagen synthesis, and stabilize RUNX2 expression (Wei et al., 2015; Guntur et al., 2018). Accordingly, molecular signals that determine osteoblast specification, such as Wnt, PTH, or Hypoxia-inducible factor 1 (HIF-1), also promote aerobic glycolysis in osteoblast progenitors (Esen et al., 2013, 2015; Regan et al., 2014; Dirckx et al., 2018). However, in the adult human skeleton, about 42 billion osteocytes are entrapped in their own mineralized matrix while being connected by cytoplasmic projections with a total length of 175,000 km. These resident osteocytes leave space for just 24 mL extracellular fluid (Buenzli and Sims,

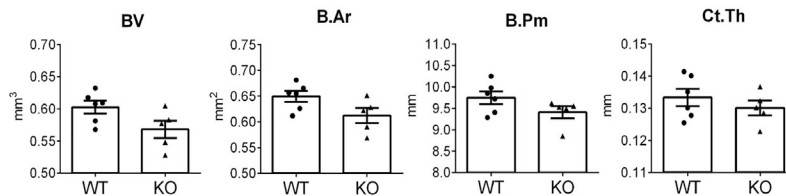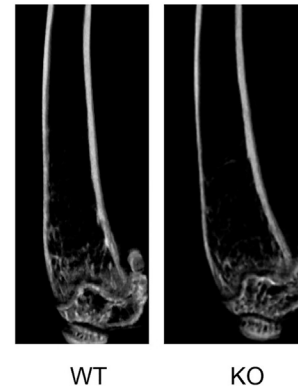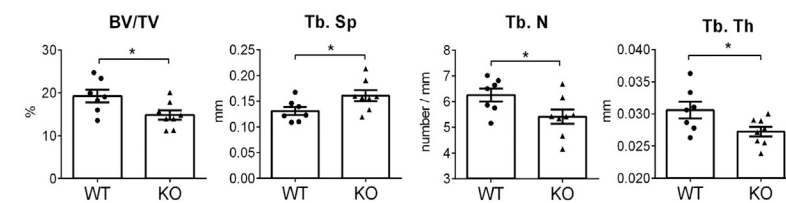**A**

Cortical analysis male
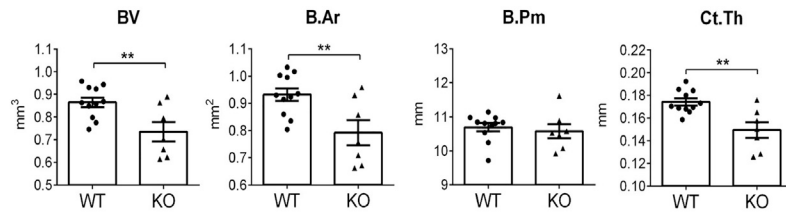
Trabecular analysis male
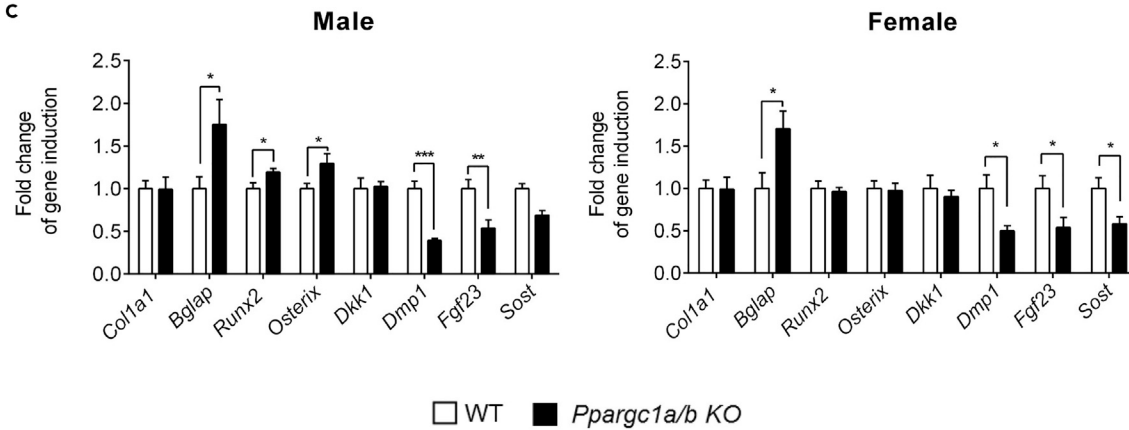

WT   KO
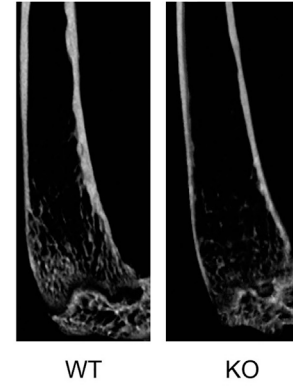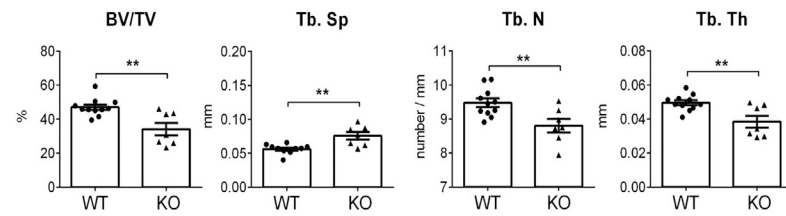
B

Cortical analysis female

Trabecular analysis female

WT   KO

C

☐ WT   ■ *Ppargc1a/b KO*

Figure 7. Bone phenotype of *Ppargc1α/β* Conditional Knockout Mice

(A and B) Micro-computed tomographic analysis and representative images of femurs obtained from male (A) and female (B) *Ppargc1a/b*^f/f;Col1a1-Cre and control (*Ppargc1a/b*^f/f) mice. Results were plotted as mean ± SEM of 8–11 independent animals.

(C) mRNA expression levels of osteocytic and osteoblastic genes in calvaria obtained from PGC1α/β conditional knockout (*Ppargc1a/b* ^f/f;Col1a1-Cre) and control mice.

Results are plotted as mean ± SEM of eight independent animals. mRNA expression levels were measured by qRT-PCR and normalized to *Tbp* expression. *p < 0.05, **p < 0.01, and ***p < 0.001 using Student's t test. B.Ar, bone area; B.Pm, bone perimeter; Ct.Th, cortical thickness; Tb.N, trabecular number; Tb.Sp, trabecular spacing; Tb.Th, trabecular thickness; See also Figures S7–S10.

2015). Therefore osteocyte transition and network formation processes are likely to demand high levels of energy in a nutrient-restricted environment. Our data demonstrate that a shift of the metabolic machinery toward a higher mitochondrial function occurs during the transition of osteoblasts into osteocytes under conditions of glucose restriction. Mitochondria optimize their morphology to cope with reduced caloric supply. Correspondingly, osteocytes *in vivo* have been shown to have numerous mitochondria and to maintain normal oxidative status through mitochondrial pathways (Frikha-Benayed et al., 2016). Osteocytes contribute little to glucose consumption in murine bones compared with osteoprogenitors and osteoblasts (Dirckx et al., 2018). Furthermore, it has been recently shown that bone accumulates a significant fraction of postprandial fatty acids and that suppression of fatty acid oxidation in mature osteoblasts and osteocytes impairs bone accrual (Kim et al., 2017). This link between metabolic reprogramming and cellular specification was already well established for other models of cell specification. For example, higher mitochondrial biogenesis and function is related to the final stage of neurogenesis, astrocytogenesis, hepatic differentiation, and erythropoiesis (Agostini et al., 2016; Xing et al., 2017). On the other hand, we also found that hyperglycemic conditions modify mitochondrial organization and impair osteoblast and osteocyte gene expression. Hyperglycemic microenvironments have been associated with a reduction in osteocyte number and function (Rinker et al., 2014), whereas bone turnover and remodeling have been found to be compromised in patients with diabetes (Kalaitzoglou et al., 2016).

Consistent with its role as regulator of energy homeostasis, we found an inverse correlation between AMPK activity and glucose supply. These results are in agreement with recent evidence showing that AMPK became activated by phosphorylation at Thr172, by sensing not only low cellular energy but also low glucose supply (Lin and Hardie, 2017; Zhang et al., 2017). Activation of AMPK with AMP analogs in normoglycemia was sufficient to induce osteocyte gene expression in IDG-SW3 cells and organotypic bone cultures. Indeed, studies using whole-body and osteoblast-specific genetic abrogation of AMPK activity showed lower cortical and trabecular bone density and enhanced bone turnover (Jeyabalan et al., 2012; Kanazawa et al., 2018). It has been shown that AMPK activation decreases *Rankl* and increases *Sost* expression in osteocytes to delicately coordinate bone turnover (Jeyabalan et al., 2012). Our data also demonstrated that activation of SIRT1 by SRT2104 led to increased osteocyte gene expression program in IDG-SW3 cells and organotypic bone cultures. An increase in bone mineral density was observed in mice fed on a diet supplemented with SRT2104 and shown to be *Sirt1* dependent (Mercken et al., 2014). The beneficial role of SIRT1 in bone formation and remodeling were further confirmed in whole-body and osteoblast-specific *Sirt1*-deficient mice, which displayed low bone mass phenotype (Cohen-Kfir et al., 2011). Moreover, SIRT1 activation gave protection against osteoporosis in both mice and humans (Ornstrup et al., 2014).

We identified a key role of PGC-1, downstream of AMPK, in the coordination of mitochondrial biogenesis and osteocyte specification in cultured cells and murine models. Lessons from other tissues indicate that PGC-1α and PGC-1β have a redundant transcriptional role because noticeable phenotypes were only observed when the expression of both co-activators was abolished (Villena, 2015). Our data show that PGC-1α/β also have a fundamental role in osteoblast and osteocyte function and bone homeostasis. *Ppargc1a* was expressed in osteoblasts and osteocytes in preference to *Ppargc1b*. Moreover, osteoblast-to-osteocyte transition further increased this tendency. Interestingly, PGC-1β is the main member of the PGC-1 family expressed in osteoclasts and is specifically required for osteoclast function (Wei et al., 2010; Zhang et al., 2018). The functional and therapeutic implications of such cell-type-specific co-activator preferences await further research. For instance, the action of different activators of PGC-1α in osteoblasts prevents bone loss in type 2 diabetes models without improving diabetes in a PGC-1α-dependent manner (Khan et al., 2015).

PGC-1 co-activates specific transcription factors, including NRF1, NRF2, PPARs, ERα, ERRα, and MEF2C (Villena, 2015). Co-activation of ERα could account for the milder osteopenic phenotypes that we

obtained in female mice because osteocyte-specific deletion of ERα has been shown to affect bone mineral density only in male mice (Lee et al., 2003; Windahl et al., 2013). Co-activation of diverse transcription factors by PGC-1 has been shown to deeply affect developmental transcriptional programs such as erythropoiesis, chondrogenesis, and differentiation of hepatocytes, cardiomyocytes, and brown adipocytes (Wanet et al., 2017; Cui et al., 2014). Our data show that this would also be the case for osteocytogenesis. For instance, PGC-1α binds to the *Fgf23* or *Sost* gene promoters, whereas overexpression and loss-of-function experiments produce effects on the expression of *Dmp1*, *Dkk1*, *Fgf23*, *Sost*, or *Osx* genes. We found numerous conserved binding sites for known transcription factors in the promoter and enhancer regions of *Fgf23*, *Sost*, *Dmp1,* or *Osx* genes that could mediate their regulation by PGC1-α. For instance, it is known that ERα, NRF2, PPARs, ERRα, and MEF2C positively regulate osteocyte gene expression (Kramer et al., 2012; Stechschulte et al., 2016). Therefore PGC-1s are able to co-activate a number of transcription factors with universal and osteocyte-specific functions. Altogether, we have uncovered a central role of PGC-1-mediated transcriptional program required for osteoblast and osteocyte function.

Limitations of Study

Our results demonstrate that glucose restriction promotes osteocytic gene expression through PGC-1-mediated transcriptional co-activation. However, at present, the transcription factors directly involved in this co-activation in specific gene promoters are still unknown and require further investigation. In addition, *Ppargc1a/b* is deleted in both osteoblasts and osteocytes in our mouse model. Therefore we are unable to distinguish the relative contribution in bone homeostasis *in vivo* of PGC-1 expressed in osteoblasts and osteocytes.

METHODS

All methods can be found in the accompanying Transparent Methods supplemental file.

SUPPLEMENTAL INFORMATION

Supplemental Information can be found online at https://doi.org/10.1016/j.isci.2019.04.015.

AUTHOR CONTRIBUTIONS

Conceived and designed the experiments: C.S.-d.-D., N.A., C.P.-L., B.T., P.M.G.-R., J.L.R., and F.V. Performed the experiments: C.S.-d.-D., N.A., C.P.-L., J.A. Valer, B.T., P.G.-P., P.M.G.-R., J.L.R., and F.V. Analyzed the data: C.S.-d.-D., N.A., C.P.-L., P.M.G.-R., J.L.R., and F.V. Contributed materials J.A. Villena. Wrote the paper: C.S.-d.-D., F.V.

DECLARATION OF INTERESTS

The authors declare no conflicts of interest.

REFERENCES

Agostini, M., Romeo, F., Inoue, S., Niklison-Chirou, M.V., Elia, A.J., Dinsdale, D., Morone, N., Knight, R.A., Mak, T.W., Melino, G., et al. (2016).

Metabolic reprogramming during neuronal differentiation. Cell Death Differ. *23*, 1502–1514.

Bonewald, L.F. (2011). The amazing osteocyte. J. Bone Miner. Res. *26*, 229–238.

Brand, M.D., and Nicholls, D.G. (2011). Assessing mitochondrial dysfunction in cells. Biochem. J. *437*, 575.

Buenzli, P.R., and Sims, N.A. (2015). Quantifying the osteocyte network in the human skeleton. Bone *75*, 144–150.

Carroll, B., and Dunlop, E.A. (2017). The lysosome: a crucial hub for AMPK and mTORC1 signalling. Biochem. J. *474*, 1453–1466.

Cassidy-Stone, A., Chipuk, J.E., Ingerman, E., Song, C., Yoo, C., Kuwana, T., Kurth, M.J., Shaw, J.T., Hinshaw, J.E., Green, D.R., et al. (2008). Chemical inhibition of the mitochondrial division dynamin reveals its role in bax/bak-dependent mitochondrial outer membrane permeabilization. Dev. Cell *14*, 193–204.

Cohen-Kfir, E., Artsi, H., Levin, A., Abramowitz, E., Bajayo, A., Gurt, I., Zhong, L., D'Urso, A., Toiber, D., Mostoslavsky, R., et al. (2011). Sirt1 is a regulator of bone mass and a repressor of sost encoding for sclerostin, a bone formation inhibitor. Endocrinology *152*, 4514–4524.

Cui, S., Tanabe, O., Lim, K.C., Xu, H.E., Zhou, X.E., Lin, J.D., Shi, L., Schmidt, L., Campbell, A., Shimizu, R., et al. (2014). PGC-1 coactivator activity is required for murine erythropoiesis. Mol. Cell. Biol. *34*, 1956–1965.

Dacquin, R., Starbuck, M., Schinke, T., and Karsenty, G. (2002). Mouse α1(I)-collagen promoter is the best known promoter to drive efficient Cre recombinase expression in osteoblast. Dev. Dyn. *224*, 245–251.

Dallas, S.L., Prideaux, M., and Bonewald, L.F. (2013). The osteocyte: an endocrine cell… and more. Endocr. Rev. *34*, 658–690.

Dirckx, N., Tower, R.J., Mercken, E.M., Vangoitsenhoven, R., Moreau-Triby, C., Breugelmans, T., Nefyodova, E., Cardoen, R., Mathieu, C., Van der Schueren, B., et al. (2018). Vhl deletion in osteoblasts boosts cellular glycolysis and improves global glucose metabolism. J. Clin. Invest. *128*, 1087–1105.

Esen, E., Chen, J., Karner, C.M., Okunade, A.L., Patterson, B.W., and Long, F. (2013). WNT-LRP5 signaling induces warburg effect through mTORC2 activation during osteoblast differentiation. Cell Metab. *17*, 745–755.

Esen, E., Lee, S.Y., Wice, B.M., and Long, F. (2015). PTH promotes bone anabolism by stimulating aerobic glycolysis via IGF signaling. J. Bone Miner. Res. *30*, 1959–1968.

Fan, M., Rhee, J., St-Pierre, J., Handschin, C., Puigserver, P., Lin, J., Jäeger, S., Erdjument-Bromage, H., Tempst, P., Spiegelman, B.M., et al. (2004). Suppression of mitochondrial respiration through recruitment of p160 myb binding protein to PGC-1α: modulation by p38 MAPK. Genes Dev. *18*, 278–289.

Frikha-Benayed, D., Basta-Pljakic, J., Majeska, R.J., and Schaffler, M.B. (2016). Regional differences in oxidative metabolism and mitochondrial activity among cortical bone osteocytes. Bone *90*, 15–22.

Galloway, C.A., Lee, H., and Yoon, Y. (2012). Mitochondrial morphology-emerging role in bioenergetics. Free Radic. Biol. Med. *53*, 2218–2228.

Gerhart-Hines, Z., Rodgers, J.T., Bare, O., Lerin, C., Kim, S.H., Mostoslavsky, R., Alt, F.W., Wu, Z., and Puigserver, P. (2007). Metabolic control of muscle mitochondrial function and fatty acid oxidation through SIRT1/PGC-1alpha. EMBO J. *26*, 1913–1923.

Gomes, L.C., Benedetto, G., and Di Scorrano, L. (2011). During autophagy mitochondria elongate, are spared from degradation and sustain cell viability. Nat. Cell Biol. *13*, 589–598.

Guntur, A.R., Gerencser, A.A., Le, P.T., DeMambro, V.E., Bornstein, S.A., Mookerjee, S.A., Maridas, D.E., Clemmons, D.E., Brand, M.D., Rosen, C.J., et al. (2018). Osteoblast like MC3T3-E1 cells prefer glycolysis for ATP production but adipocyte like 3T3-L1 cells prefer oxidative phosphorylation. J. Bone Miner. Res. *33*, 1052–1065.

Guo, D., Keightley, A., Guthrie, J., Veno, P.A., Harris, S.E., and Bonewald, L.F. (2010). Identification of osteocyte-selective proteins. Proteomics *10*, 3688–3698.

Hardie, D.G. (2018). Keeping the home fires burning: AMP-activated protein kinase. J. R. Soc. Interface *15*, https://doi.org/10.1098/rsif.2017.0774.

Hirao, M., Hashimoto, J., Yamasaki, N., Ando, W., Tsuboi, H., Myoui, A., and Yoshikawa, H. (2007). Oxygen tension is an important mediator of the transformation of osteoblasts to osteocytes. J. Bone Miner. Metab. *25*, 266–276.

Jager, S., Handschin, C., St-Pierre, J., and Spiegelman, B.M. (2007). AMP-activated protein kinase (AMPK) action in skeletal muscle via direct phosphorylation of PGC-1. Proc. Natl. Acad. Sci. U S A *104*, 12017–12022.

Jeyabalan, J., Shah, M., Viollet, B., and Chenu, C. (2012). AMP-activated protein kinase pathway and bone metabolism. J. Endocrinol. *212*, 277–290.

Kalaitzoglou, E., Popescu, I., Bunn, R.C., Fowlkes, J.L., and Thrailkill, K.M. (2016). Effects of type 1 diabetes on osteoblasts, osteocytes, and osteoclasts. Curr. Osteoporos. Rep. *14*, 310–319.

Kanazawa, I., Takeno, A., Tanaka, K.I., Notsu, M., and Sugimoto, T. (2018). Osteoblast AMP-activated protein kinase regulates postnatal skeletal development in male mice. Endocrinology *159*, 597–608.

Karsenty, G., and Olson, E.N. (2016). Bone and muscle endocrine functions: unexpected paradigms of inter-organ communication. Cell *164*, 1248–1256.

Khan, M.P., Singh, A.K., Joharapurkar, A.A., Yadav, M., Shree, S., Kumar, H., Gurjar, A., Mishra, J.S., Tiwari, M.C., Nagar, G.K., et al. (2015). Pathophysiological mechanism of bone loss in type 2 diabetes involves inverse regulation of osteoblast function by pgc-1a and skeletal muscle atrogenes: adipor1 as a potential target for reversing diabetes-induced osteopenia. Diabetes *64*, 2609–2623.

Kim, S.P., Li, Z., Zoch, M.L., Frey, J.L., Bowman, C.E., Kushwaha, P., Ryan, K.A., Goh, B.C., Scafidi, S., Pickett, J.E., et al. (2017). Fatty acid oxidation by the osteoblast is required for normal bone acquisition in a sex- and diet-dependent manner. JCI insight *2*, https://doi.org/10.1172/jci.insight.92704.

Kramer, I., Baertschi, S., Halleux, C., Keller, H., and Kneissel, M. (2012). Mef2c deletion in osteocytes results in increased bone mass. J. Bone Miner. Res. *27*, 360–373.

Lai, X., Price, C., Modla, S., Thompson, W.R., Caplan, J., Kirn-Safran, C.B., and Wang, L. (2015). The dependences of osteocyte network on bone compartment, age, and disease. Bone Res. *3*, https://doi.org/10.1038/boneres.2015.9.

Lee, K., Jessop, H., Suswillo, R., Zaman, G., and Lanyon, L. (2003). Endocrinology: bone adaptation requires oestrogen receptor-α. Nature *424*, 389.

Lin, S.C., and Hardie, D.G. (2017). AMPK: sensing glucose as well as cellular energy status. Cell Metab. *27*, 299–313.

Mercken, E.M., Mitchell, S.J., Martin-Montalvo, A., Minor, R.K., Almeida, M., Gomes, A.P., Scheibye-Knudsen, M., Palacios, H.H., Licata, J.J., Zhang, Y., et al. (2014). SRT2104 extends survival of male mice on a standard diet and preserves bone and muscle mass. Aging Cell *13*, 787–796.

Napoli, N., Chandran, M., Pierroz, D.D., Abrahamsen, B., Schwartz, A.V., and Ferrari, S.L.; IOF Bone and Diabetes Working Group (2017). Mechanisms of diabetes mellitus-induced bone fragility. Nat. Rev. Endocrinol. *13*, 208–219.

Ornstrup, M.J., Harsløf, T., Kjær, T.N., Langdahl, B.L., and Pedersen, S.B. (2014). Resveratrol increases bone mineral density and bone alkaline phosphatase in obese men: a randomized placebo-controlled trial. J. Clin. Endocrinol. Metab. *99*, 4720–4729.

Petrov, N., and Pollack, S.R. (2003). Comparative analysis of diffusive and stress induced nutrient transport efficiency in the lacunar-canalicular system of osteons. Biorheology *40*, 347–353.

Piekarski, K., and Munro, M. (1977). Transport mechanism operating between blood supply and osteocytes in long bones. Nature *269*, 80–82.

Quinn, J.M.W., Tam, S., Sims, N.A., Saleh, H., McGregor, N.E., Poulton, I.J., Scott, J.W., Gillespie, M.T., Kemp, B.E., van Denderen, B.J.W., et al. (2010). Germline deletion of AMP-activated protein kinase ;? subunits reduces bone mass without altering osteoclast differentiation or function. FASEB J. *24*, 275–285.

Regan, J.N., Lim, J., Shi, Y., Joeng, K.S., Arbeit, J.M., Shohet, R.V., and Long, F. (2014). Up-regulation of glycolytic metabolism is required for HIF1 -driven bone formation. Proc. Natl. Acad. Sci. U S A *111*, 8673–8678.

Riddle, R.C., and Clemens, T.L. (2017). Bone cell bioenergetics and skeletal energy homeostasis. Physiol. Rev. *97*, 667–698.

Rinker, T.E., Hammoudi, T.M., Kemp, M.L., Lu, H., and Temenoff, J.S. (2014). Interactions between mesenchymal stem cells, adipocytes, and osteoblasts in a 3D tri-culture model of hyperglycemic conditions in the bone marrow microenvironment. Integr. Biol. *6*, 324–337.

Sato, M., Asada, N., Kawano, Y., Wakahashi, K., Minagawa, K., Kawano, H., Sada, A., Ikeda, K., Matsui, T., and Katayama, Y. (2013). Osteocytes regulate primary lymphoid organs and fat metabolism. Cell Metab. *18*, 749–758.

Stechschulte, L.A., Czernik, P.J., Rotter, Z.C., Tausif, F.N., Corzo, C.A., Marciano, D.P., Asteian, A., Zheng, J., Bruning, J.B., Kamenecka, T.M., et al. (2016). PPARG post-translational modifications regulate bone formation and bone resorption. EBioMedicine *10*, 174–184.

Villena, J.A. (2015). New insights into PGC-1 coactivators: redefining their role in the regulation of mitochondrial function and beyond. FEBS J. *282*, 647–672.

Wanet, A., Caruso, M., Domelevo Entfellner, J.B., Najar, M., Fattaccioli, A., Demazy, C., Evraerts, J., El-Kehdy, H., Pourcher, G., Sokal, E., et al. (2017). The transcription factor 7-like 2–peroxisome proliferator-activated receptor gamma coactivator-1 alpha axis connects mitochondrial biogenesis and metabolic shift with stem cell commitment to hepatic differentiation. Stem Cells *35*, 2184–2197.

Wang, L. (2018). Solute transport in the bone lacunar-canalicular system (LCS). Curr. Osteoporos. Rep. *16*, 32–41.

Wei, J., Shimazu, J., Makinistoglu, M.P., Maurizi, A., Kajimura, D., Zong, H., Takarada, T., Lezaki, T., Pessin, J.E., Hinoi, E., et al. (2015). Glucose Uptake and runx2 synergize to orchestrate osteoblast differentiation and bone formation. Cell *161*, 1576–1591.

Wei, W., Wang, X., Yang, M., Smith, L.C., Dechow, P.C., Sonoda, J., Evans, R.M., and Wan, Y. (2010). PGC1beta mediates PPARgamma activation of osteoclastogenesis and rosiglitazone-induced bone loss. Cell Metab. *11*, 503–516.

Windahl, S.H., Börjesson, A.E., Farman, H.H., Engdahl, C., Movérare-Skrtic, S., Sjögren, K., Lagerquist, M.K., Kindblom, J.M., Koskela, A., Tuukkanen, J., et al. (2013). Estrogen receptor- in osteocytes is important for trabecular bone formation in male mice. Proc. Natl. Acad. Sci. U S A *110*, 2294–2299.

Woo, S.M., Rosser, J., Dusevich, V., Kalajzic, I., and Bonewald, L.F. (2011). Cell line IDG-SW3 replicates osteoblast-to-late-osteocyte differentiation in vitro and accelerates bone

formation in vivo. J. Bone Miner. Res. *26*, 2634–2646.

Xing, F., Luan, Y., Cai, J., Wu, S., Mai, J., Gu, J., Zhang, H., Li, K., Lin, Y., Xiao, X., et al. (2017). The anti-warburg effect elicited by the camp-pgc1α pathway drives differentiation of glioblastoma cells into astrocytes. Cell Rep. *18*, 468–481.

Yu, T., Robotham, J.L., and Yoon, Y. (2006). Increased production of reactive oxygen species in hyperglycemic conditions requires dynamic change of mitochondrial morphology. Proc. Natl. Acad. Sci. U S A *103*, 2653–2658.

Zhang, C.S., Hawley, S.A., Zong, Y., Li, M., Wang, Z., Gray, A., Ma, T., Cui, J., Feng, J.W., Zhu, M., et al. (2017). Fructose-1,6-bisphosphate and aldolase mediate glucose sensing by AMPK. Nature *548*, 112–116.

Zhang, Y., Rohatgi, N., Veis, D.J., Schilling, J., Teitelbaum, S.L., and Zou, W. (2018). PGC1beta organizes the osteoclast cytoskeleton by mitochondrial biogenesis and activation. J. Bone Miner. Res. *33*, 1114–1125.
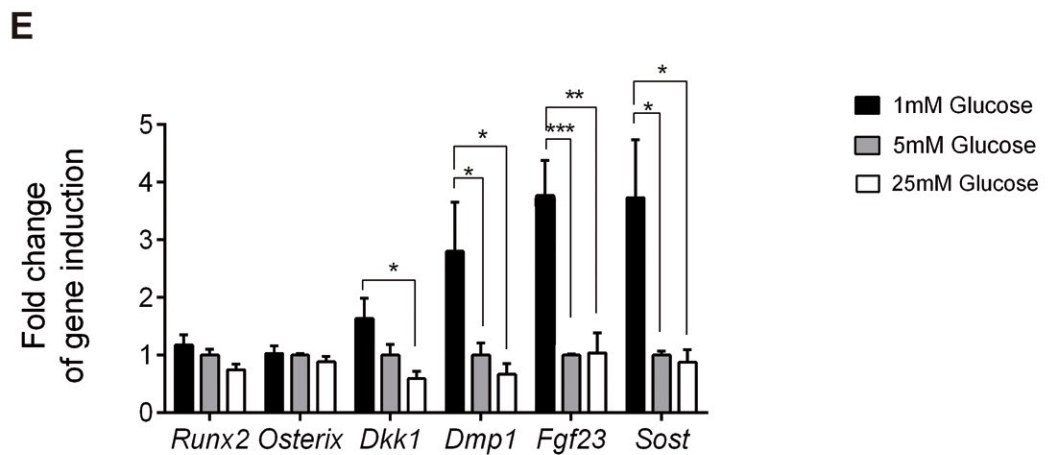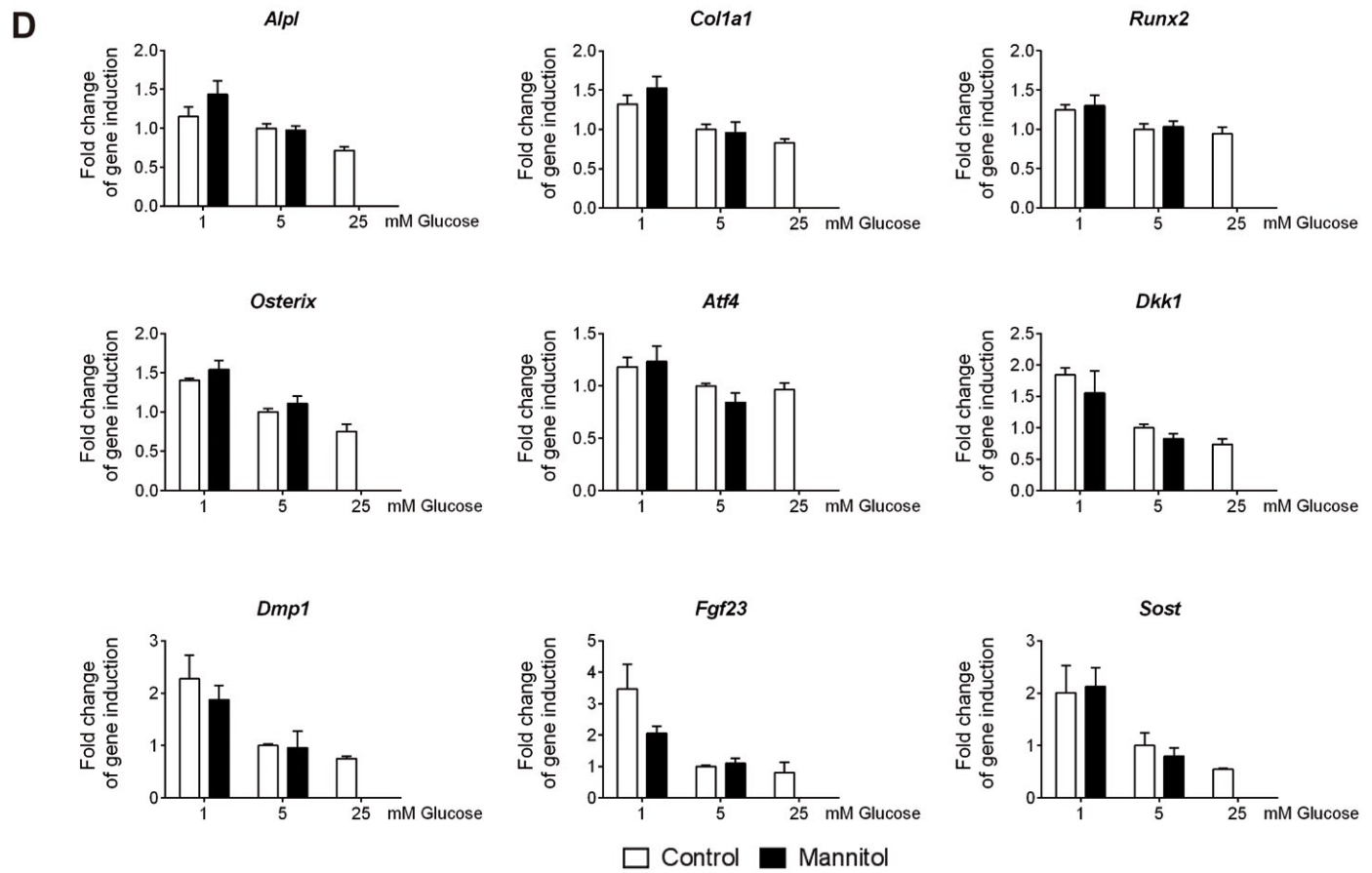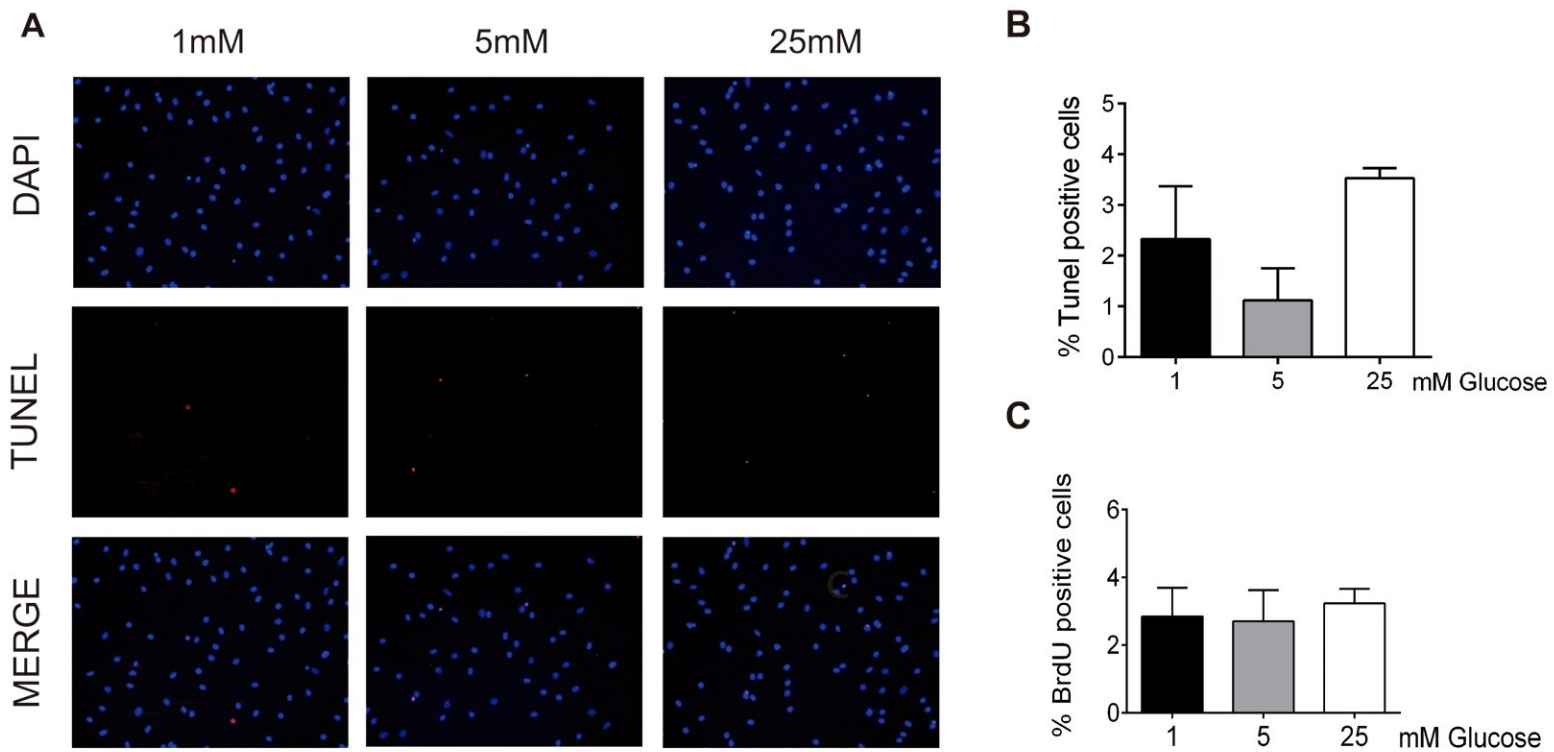
Supplemental Information

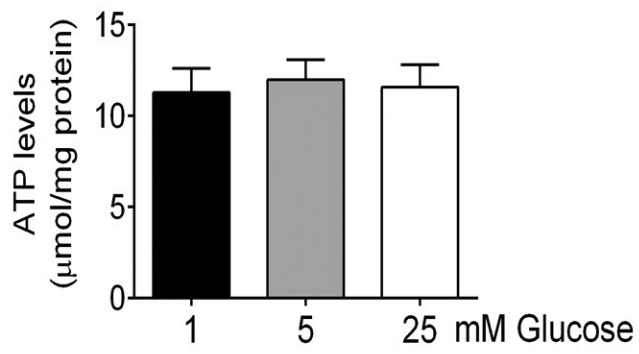**Glucose Restriction Promotes Osteocyte**

Specification by Activating
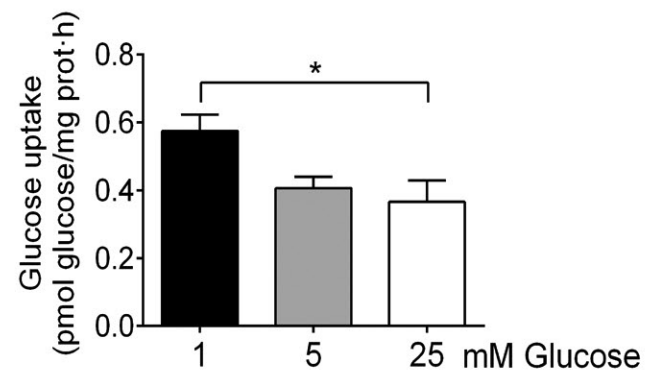
a PGC-1α-Dependent Transcriptional Program

Cristina Sánchez-de-Diego, Natalia Artigas, Carolina Pimenta-Lopes, José Antonio Valer, Benjamin Torrejon, Pau Gama-Pérez, Josep A. Villena, Pablo M. Garcia-Roves, José Luis Rosa, and Francesc Ventura
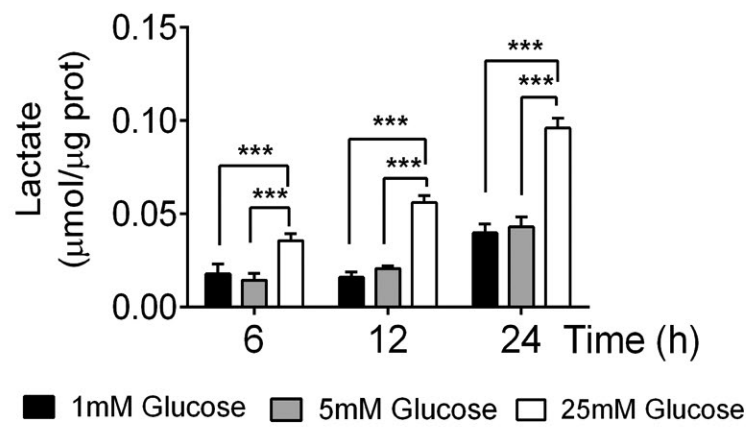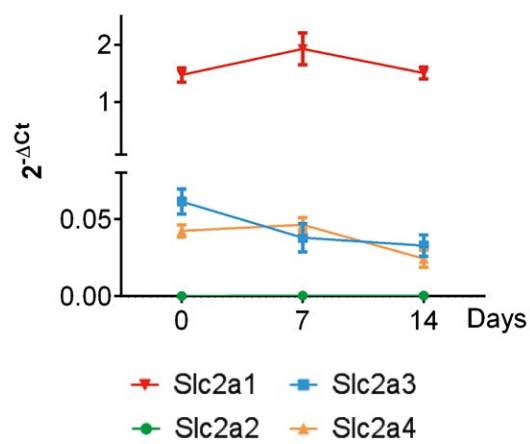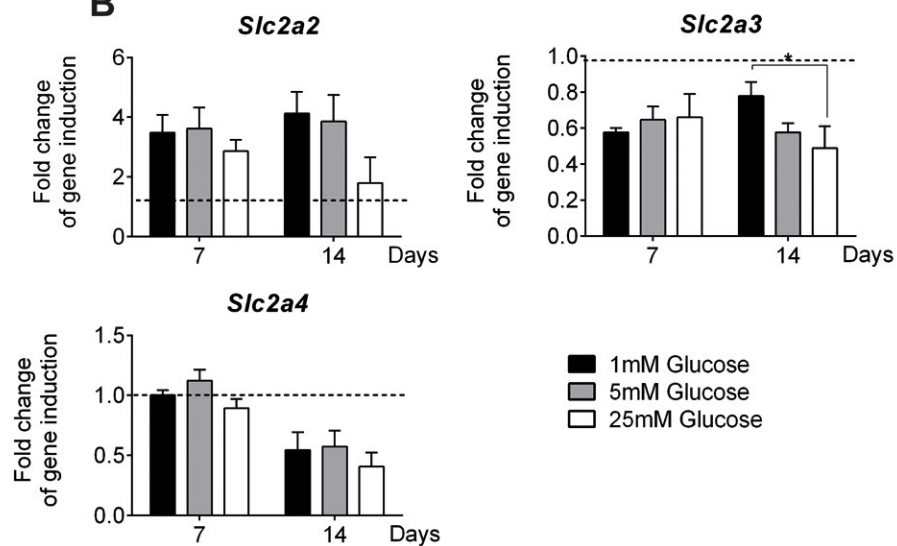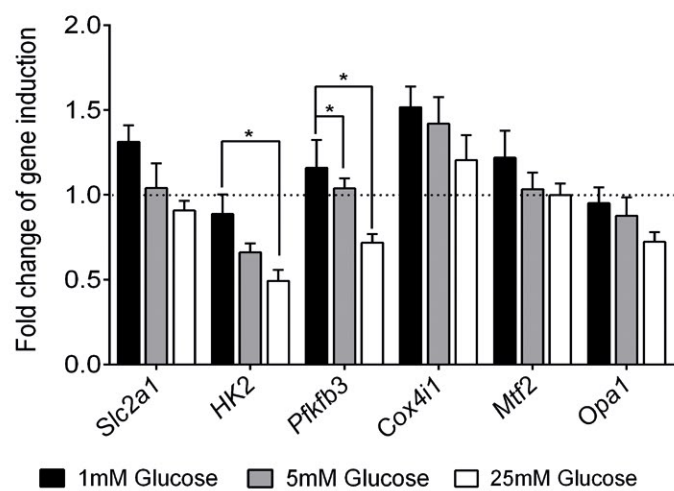
Suppl. Figure 1

A

	1mM	5mM	25mM
DAPI			
TUNEL			
MERGE			

B

C

D

Alpl *Col1a1* *Runx2*

Osterix *Atf4* *Dkk1*

Dmp1 *Fgf23* *Sost*

□ Control   ■ Mannitol

E

Suppl. Figure 2

A

B

C

Suppl. Figure 3

A

B *Slc2a2* *Slc2a3*

Slc2a4

■ 1mM Glucose
■ 5mM Glucose
□ 25mM Glucose

C

■ 1mM Glucose ■ 5mM Glucose □ 25mM Glucose

D

E Glucose
1mM 5mM 25mM

CV-ATP5A
CIII-UQCRC2
CIV-MTCO1
CI-NDUFB8
α-Tubulin

F Mitotracker Zoom

1mM

10 µm 5 µm

5mM

10 µm 5 µm

25mM

10 µm 5 µm

Suppl. Figure 4

A

6h   12h   24h

1   5   25   1   5   25   1   5   25   mM Glucose

pp38

peif2α

pS6

ATF4

Sirt1

pAMPK

pACC

Pgc1-α

α-Tubulin

B

10 days

1   5   25   mM Glucose

pp38

peif2α

pS6

ATF4

Sirt1

pAMPK

pACC

α-Tubulin

C

Fold change of gene induction

10
8
6
4
2
1
0

Ppargc1a   *Ppargc1b*   *Sirt1*

*

*

☐ 1mM glucose   ▤ 5mM glucose   ■ 25mM glucose

Suppl. Figure 5

A

	DAPI	TUNEL	MERGE
WT			
Ppargc1a/b KO			
Control +			

B

% Tunel positive cells

C

% BrdU positive cells

D

	1mM	5mM	25mM
WT			
Ppargc1a/b KO			

20 µm

E

Relative mtDNA expression

**

☐ WT
■ *Ppargc1a/b KO*

1   5   25   mM Glucose

Suppl. Figure 6

A

IDG-SW3

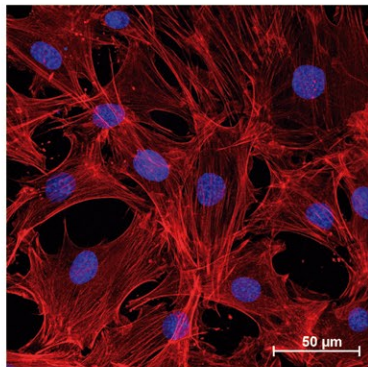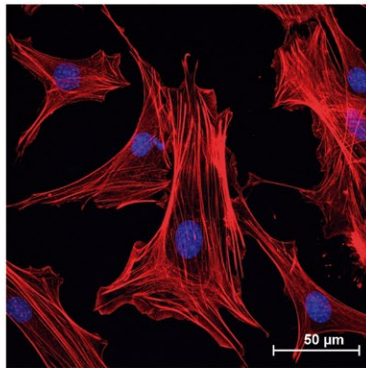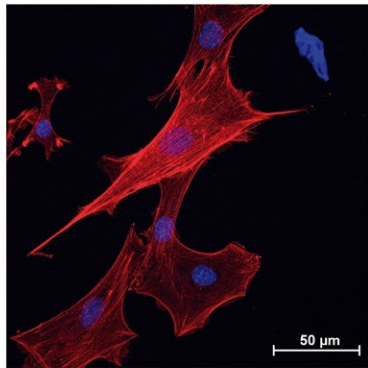1mM   5mM   25mM

B   **Osteoblasts**

WT   *Ppargc1a/b* KO
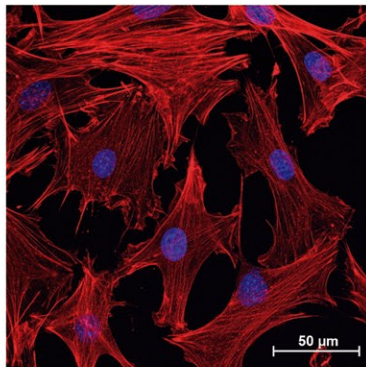
C   **Osteocytes**

WT   *Ppargc1a/b* KO

Suppl. Figure 7

A Osteoblasts

Ppargc1a

Ppargc1b

B Osteocytes

Ppargc1a

Ppargc1b

C Male Calvariae

Ppargc1a

Ppargc1b

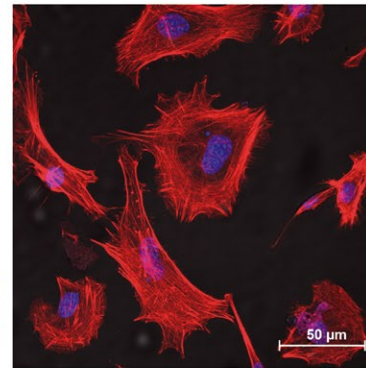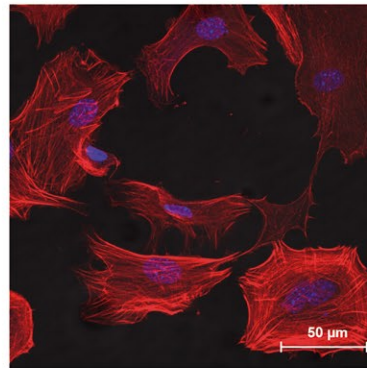**D** Female Calvariae

Ppargc1a

Ppargc1b

A

B
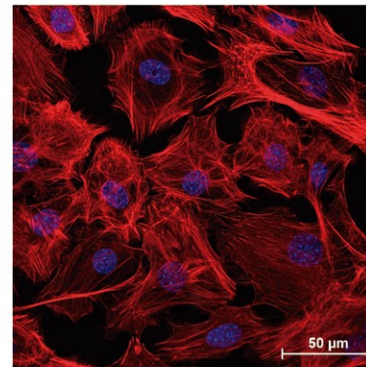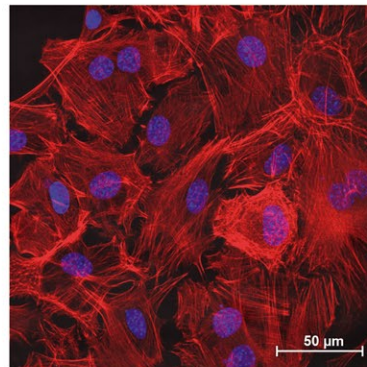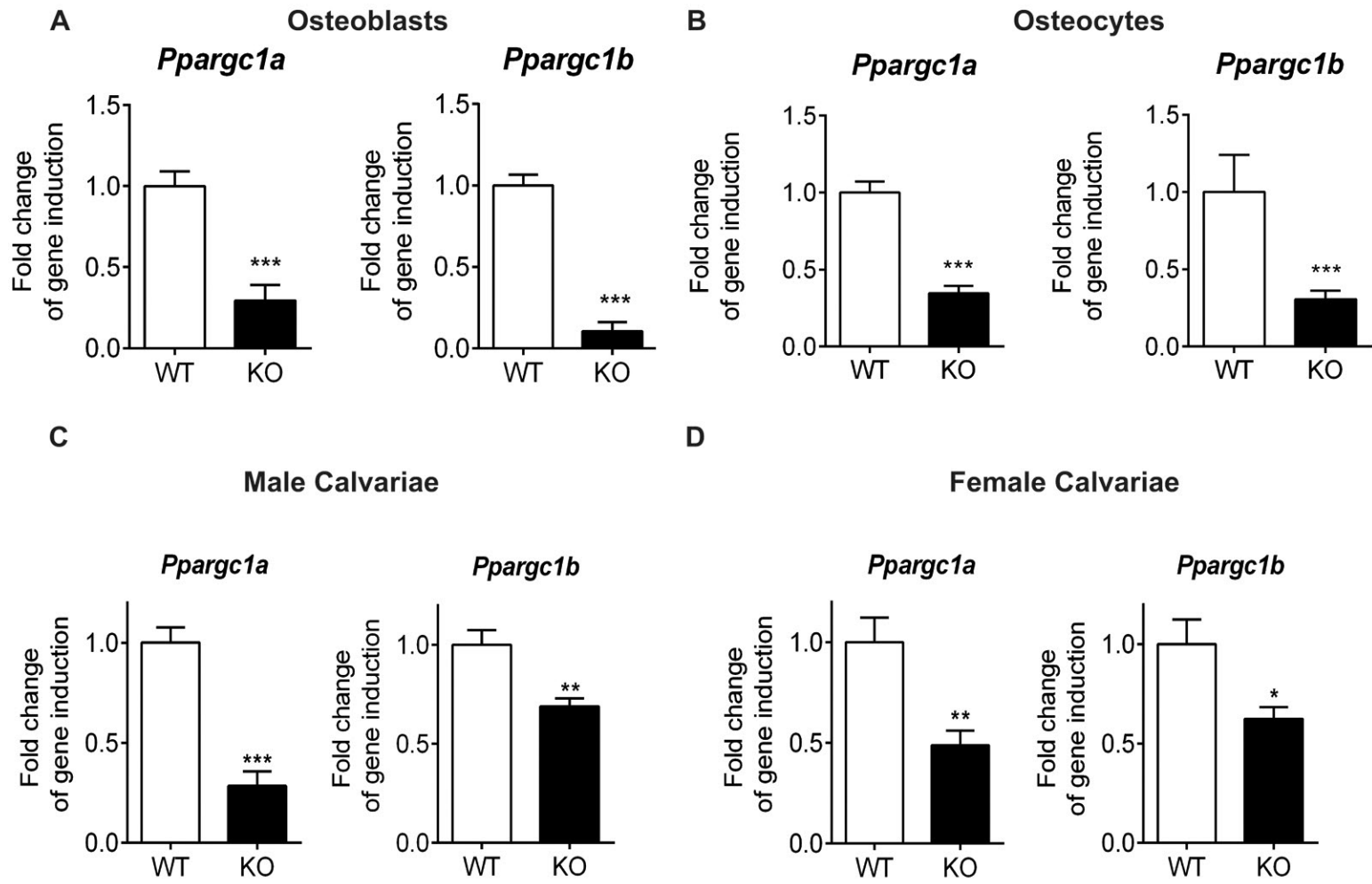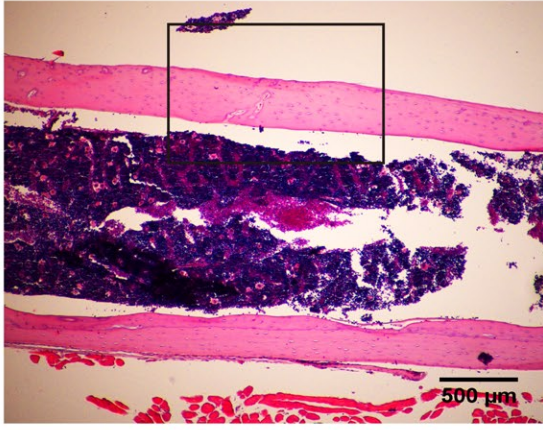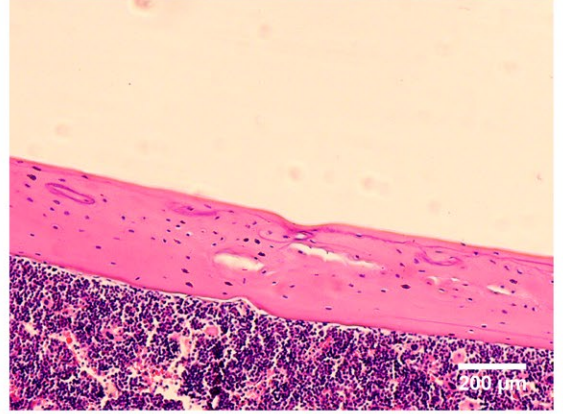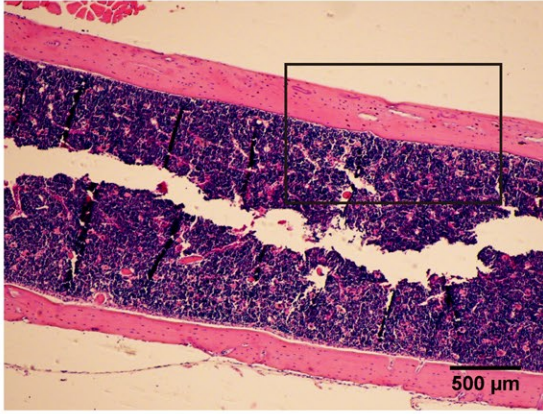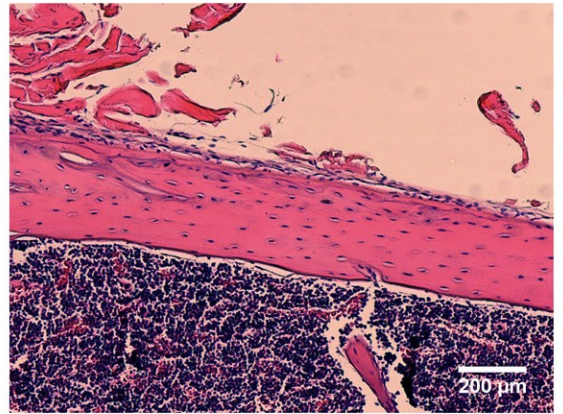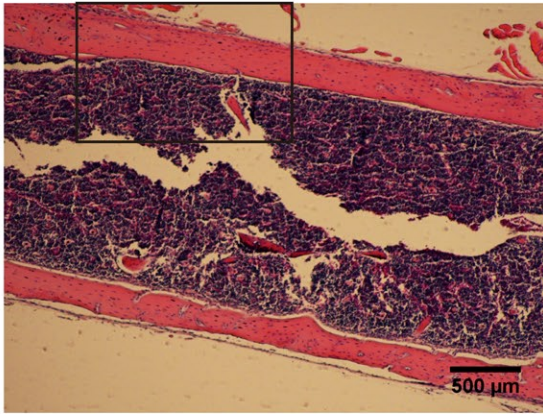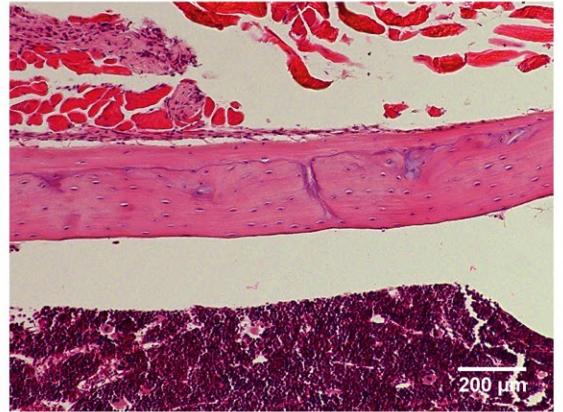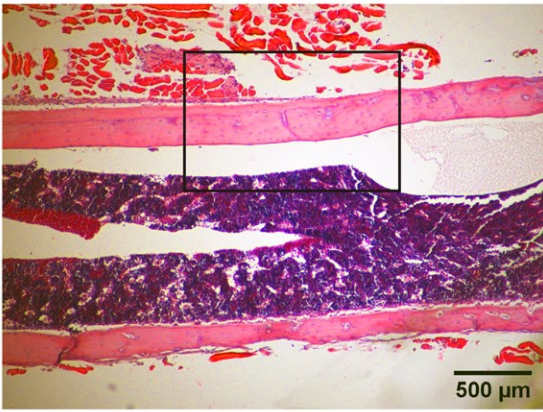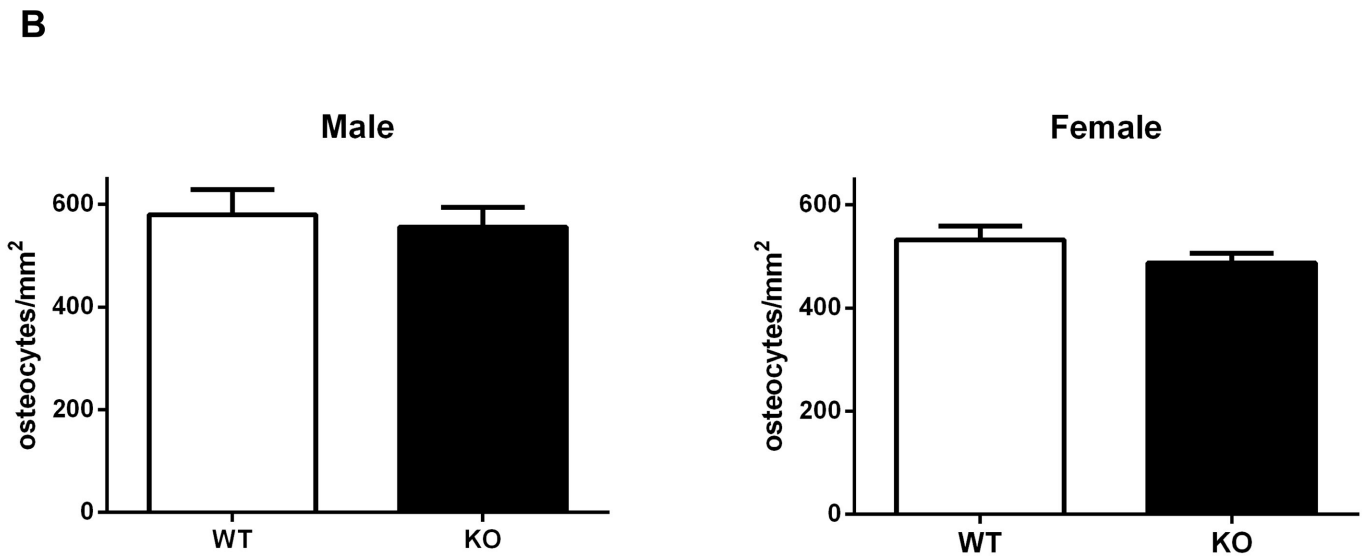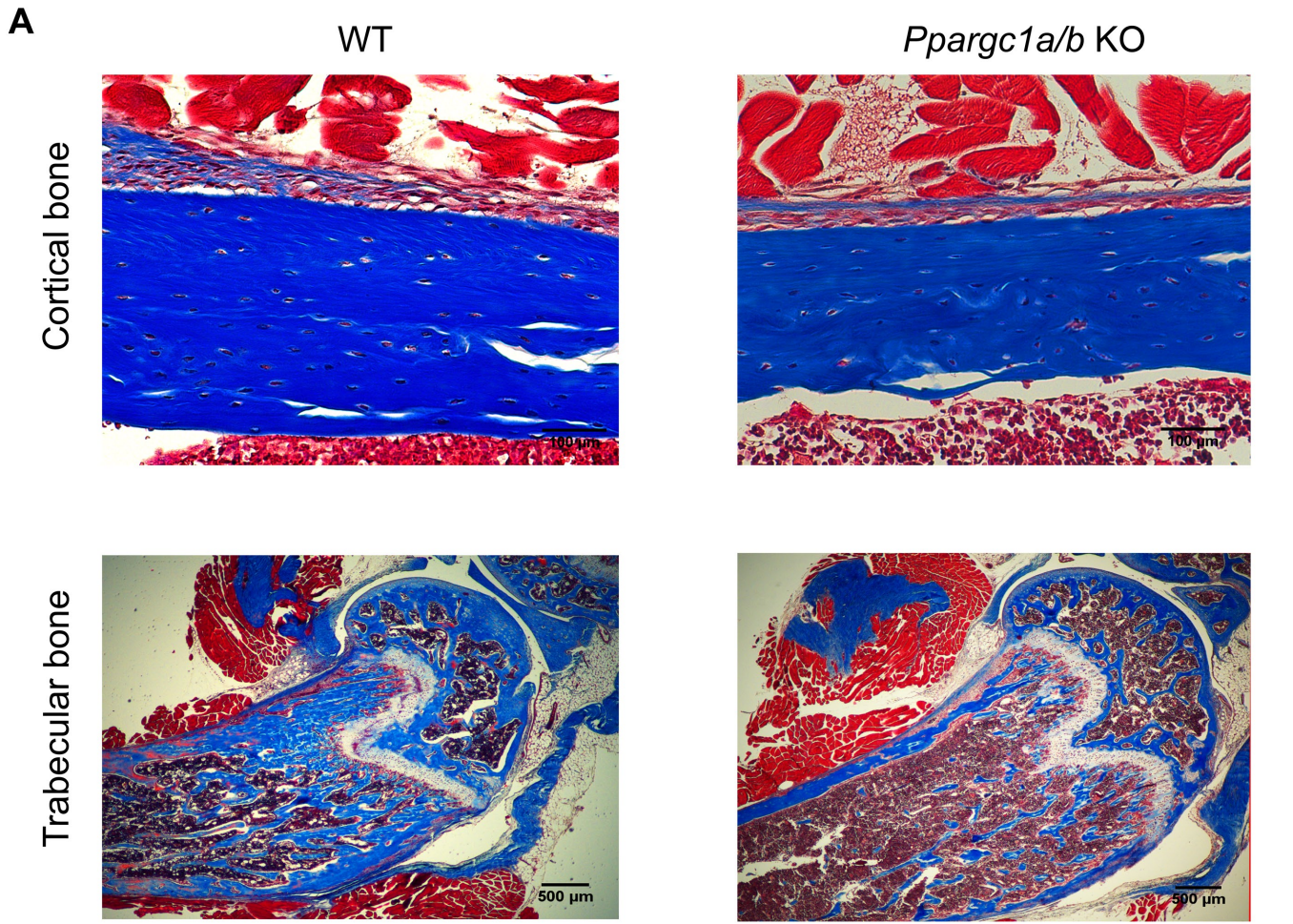
A

Osteocytes
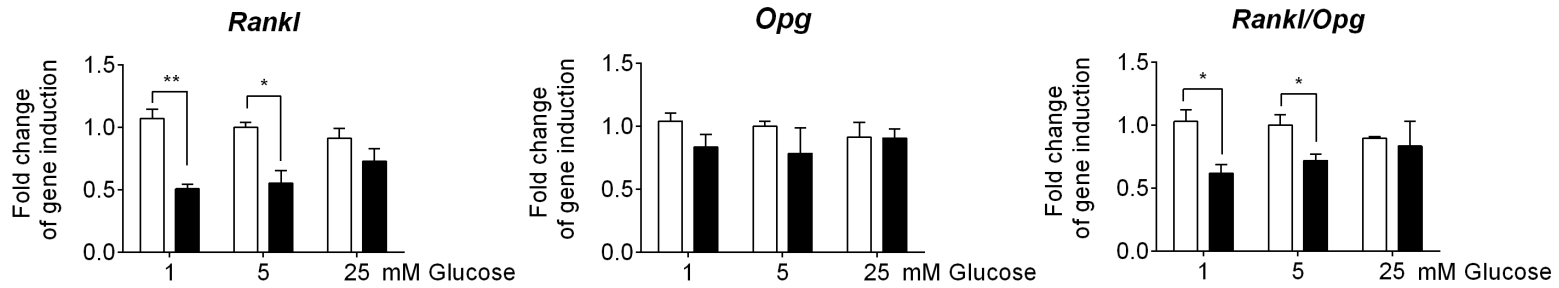
B

Male Calvaria

C
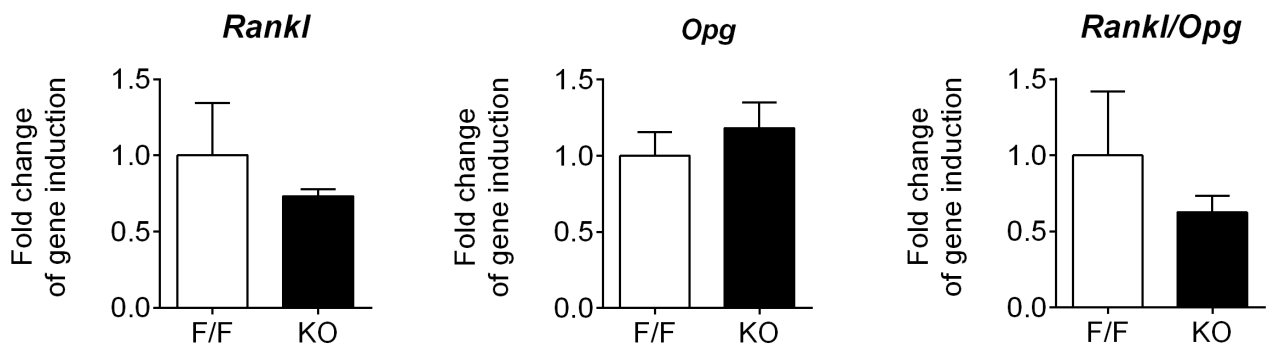
Female Calvaria
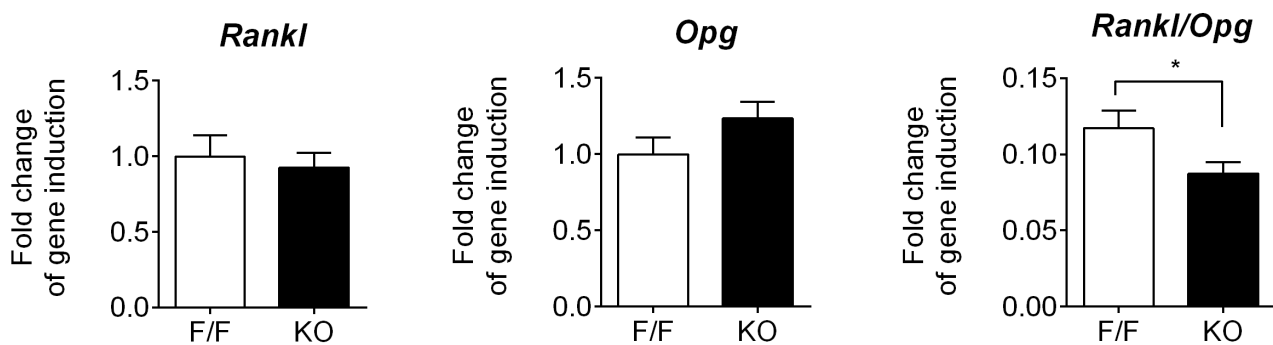
Figure S1. Glucose supply is responsible for changes in gene expression, related to Figure 1. (A and B) TUNEL staining of IDG-SW3 differentiated for 14 days in the presence of 1, 5 or 25 mM glucose. Representative images (A) and quantitative analysis (B) of TUNEL staining. Results are plotted as mean ± SEM of three independent experiments. (C) Proliferation rate of IDG-SW3 differentiated for 14 days in presence of 1, 5 or 25 mM glucose. Results are expressed as percentage of BrdU$^+$ cells. Data are plotted as mean ± SEM of three independent experiments. (D) Quantification of mRNA expression levels in IDG-SW3 cells differentiated for 14 days in the presence of 1, 5 or 25 mM glucose or in the presence of 1mM glucose plus 24 mM mannitol and 5 mM glucose plus 20 mM mannitol. Results are plotted as expression relative to IDG-SW3 cells cultured in 5 mM glucose and statistical analysis was performed between conditions with or without mannitol (E) Quantification of mRNA expression levels in organotypic cultures from mouse femur maintained in 1, 5 or 25 mM glucose media. Results are plotted as expression relative to organotypic cultured maintained in 5 mM glucose media. mRNA levels were measured by RT-qPCR and normalized to *Tbp* expression. Results are plotted as mean ± SEM of six independent experiments. *$p<0.05$, **$p<0.01$ and ***$p<0.001$ using Student´s t-test.

Figure S2. Metabolic profile in primary mature osteoblasts under different glucose supplies, Related to Figure 2. (A) ATP levels in osteoblasts after 10 days of differentiation in the presence of 1, 5 or 25 mM glucose. (B) Determination of the maximal uptake capacity for glucose in osteoblast differentiated for 10 days in the presence of 1, 5 or 25 mM glucose. Glucose uptake was tested at 10 µM glucose for all conditions. (C) Quantification of lactate release in osteoblasts differentiated for 10 days in the presence of 1, 5 or 25 mM glucose.

Figure S3. Changes in glycolytic gene expression and mitochondrial function induced by different glucose concentrations, Related to Figure 3. (A) mRNA expression levels of the different GLUT family members (SLC2a) in IDG-SW3 differentiated for 14 days in 5 mM glucose media. mRNA expression was quantified by RT-qPCR and normalized to *Tbp* expression. Results are plotted as 2-ΔCt (mean ± SEM of six independent experiments). (B) mRNA expression levels of *Slc2a2, Slc2a3 and Slc2a4* during IDG-SW3 differentiation in 1, 5 and 25 mM glucose media. mRNA levels were quantified by qRT-PCR, normalized by *Tbp* and plotted as expression relative to undifferentiated IDG-SW3 (mean ± SEM of six independent experiments). (C) mRNA expression levels of glycolytic and mitochondrial genes in primary osteoblasts differentiated for 10 days in the presence of 1, 5 or 25 mM glucose. Results are plotted as expression relative to undifferentiated primary osteoblasts (mean ± SEM of six independent experiments). (D) Quantification of mtDNA in primary osteoblasts differentiated for 10 days in the presence of 1, 5 or 25 mM glucose. Results are plotted as expression relative to undifferentiated primary osteoblasts (mean ± SEM of four independent experiments). (E) Analysis of the levels of mitochondrial complexes in primary osteoblasts differentiated for 10 days in the presence of 1, 5 or 25 mM glucose. (F) Visualization of mitochondria in primary osteoblasts differentiated for 10 days in the presence of 1, 5 or 25 mM glucose. $*p<0.05$, $**p<0.01$ and $***p<0.001$ using one-way ANOVA.

Figure S4. Signaling pathways involved in glucose restriction in osteoblasts, Related to Figure 4 and 5. (A and B) Immunoblots from primary osteoblasts during the first 24 hours of differentiation in 1, 5 or 25 mM glucose media (A) or after 10 days of differentiation in 1, 5 and 25 mM glucose media (B). (C) mRNA expression levels of *Ppargc1* isoforms and *Sirt1* in primary osteoblasts differentiated for 10 days in 1, 5 or 25

mM glucose media. Results are plotted as ΔΔCt relative to undifferentiated osteoblasts at day 0 (mean ± SEM of five independent experiments).

Figure S5. Loss of PGC-1α/β does not affect cell viability but abolishes the increase in mitochondrial DNA induced by glucose restriction, Related to Figure 6. (A and B) TUNEL staining of primary osteoblasts wild-type (WT) and knock-out (KO) for *Ppargc1a/b*. Representative images (A) and quantitative analysis (B) of TUNEL staining. Results are plotted as mean ± SEM of three independent experiments. (C) Proliferation rate of primary osteoblasts wild-type and KO for *Ppargc1a/b*. Results are expressed as percentage of $BrdU^+$ cells. Data are plotted as mean ± SEM of three independent experiments. (D) Visualization of mitochondria in primary osteoblasts wild-type and KO for *Ppargc1a/b* differentiated for 10 days in the presence of 1, 5 or 25 mM glucose. (E) Quantification of mtDNA in primary osteoblasts, wild-type and KO for *Ppargc1a/b*, differentiated for 10 days in the presence of 1, 5 or 25 mM glucose. Results are plotted relative to the content of wild type osteoblasts cultures at 5 mM glucose as mean ± SEM of four independent experiments. $*p<0.05$, $**p<0.01$ and $***p<0.001$ using one-way ANOVA.

Figure S6. Different glucose supply or deletion of *Ppgarc1a* and *Ppgarc1b* does not alter actin cytoskeleton organization, Related to Figure 6. (A) Representative images of Maximum Intensity Projection of IDG-SW3 differentiated in 1, 5, or 25 mM glucose media for 14 days and stained with Alexa 488-phalloidin (red) and DAPI (blue) (B) Maximum Intensity Projection of primary osteoblasts wild-type and KO for *Ppargc1a/b* stained with Alexa 488-phalloidin (red) and DAPI (blue) (C) Maximum Intensity Projection of primary osteocytes wild-type and KO for *Ppargc1a/b* stained with Alexa 488-phalloidin (red) and DAPI (blue).

Figure S7. *Ppgarc1a* **and** *Ppgarc1b* **expression levels in** *Ppargc1a/b* **deficient** (**KO)** **mice, Related to Figure 7.** (A). mRNA expression levels of *Ppgarc1a* and *Ppgarc1b* in primary osteoblast wild-type and KO for *Ppargc1a/b*. Results were plotted as mean ± SEM of six independent experiments. (B) mRNA expression levels of *Ppgarc1a* and *Ppgarc1b* in primary osteocytes wild-type and KO for *Ppargc1a/b*. Results were plotted as mean ± SEM of six independent experiments. (C and D) mRNA expression levels of *Ppgarc1a* and *Ppgarc1b* in calvaria obtained from *Ppargc1a/b* conditional knockout (*Ppargc1a/b* $^{f/f}$;Col1a1-Cre) and control male (C) and female (D) mice. Results were plotted as mean ± SEM of eight independent animals. mRNA expression levels were measured by RT-qPCR and normalized to *Tbp* expression. *p<0.05, **p<0.01 and ***p<0.001 using Student´s t-test.

Figure S8. Histological analysis of femurs of *Ppgarc1a* **and** *Ppgarc1b***-deficient mice, Related to Figure 7.** Representative images of longitudinal sections of femur from wild type (WT) and *Ppargc1a/b* knock-out (KO) mice stained with hematoxylin and eosin. Images were taken at 4x and 10x magnification.

Figure S9, Related to Figure 7. (A) Representative images of longitudinal sections from middle and distal femur from wild type (WT) and *Ppargc1a/b* knock-out (KO) mice stained with Masson's trichrome stain. Images were taken at 2x and 20x magnification. (B) Osteocyte number normalized by bone area. Results are shown as mean ± SEM of 12 different fields from 8 different animals.

Figure S10, Related to Figure 7. (A) mRNA expression levels of *Rankl*, *Opg* and *Rank*l/Opg expression ratio in primary osteocytes wild-type and KO for *Ppargc1a/b* cultured in 1, 5, and 25 mM glucose media. Results were plotted as mean ± SEM of three independent experiments. (B and C) mRNA expression levels of *Rankl*, *Opg* and the

*Rank*l/Opg expression ratio in calvaria obtained from *Ppargc1a/b* conditional knockout (*Ppargc1a/b* ^{*f/f*};Col1a1-Cre) and control male (B) and female (C) mice.

TRANSPARENT METHODS

Cell cultures

IDG-SW3 cells (obtained from Dr. L. Bonewald) were cultured as previously described [7]. Briefly, IDG-SW3 were maintained and expanded in proliferative conditions (33°C in αMEM with 5 mM glucose, 10% FBS, 2 mM glutamine, 1 mM pyruvate, 100 U/ml penicillin, 0.1 mg/ml streptomycin and 50 U/ml IFN-γ) on type I collagen-coated plates. To induce osteogenesis, cells were seeded on type I collagen-coated plates and cultured in osteogenic media (37°C in αMEM with 10% FBS, 1, 5, or 25 mM glucose, 2 mM glutamine, 1 mM pyruvate, 100 U/ml penicillin and 0.1 mg/ml streptomycin with 50 µg/ml ascorbic acid and 4 mM β-glycerophosphate, in the absence of IFN-γ).

Primary osteoblasts were isolated from calvaria as previously described [24]. Briefly, calvaria was dissected from P1-P4 pups, and sutures and soft tissue were discarded. A total of 5 to 10 calvariae were pooled and serially digested in α-MEM, containing trypsin (0.025%)/collagenase II (1 mg/mL). The product of the first 5 minutes of digestion was discarded, while the product of a double 20-minute digestion was centrifuged and seeded on 60-mm culture plates. Cells were used between passages 4 to 6. Osteoblasts were cultured in osteogenic media (as above) and the concentration of glucose adjusted to 1, 5, or 25 mM.

For bone organotypic cultures, bone pieces from mice femurs were digested in DMEM containing collagenase II (1mg/ml) for 2h at 37ºC in a shaking water bath. Then, bone pieces were rinsed, plated and incubated overnight in osteogenic media. The next day, bone pieces were washed 4 times with PBS and incubated in osteogenic media for 5 days.

Primary osteocytes were isolated with a protocol derived from Shah et al. (Shah et al. 2016, Bonekey Rep. 5:838). Briefly, mice limbs (tibiae, femur and humeri) and calvariae from 5 mice were pooled, cut and serially digested on a rotating shaker at 37°C. Bone pieces were incubated in collagenase solution (trypsin (0.025%)/collagenase II (1 mg/mL) in α-MEM) for 25 min. The solution was discarded, and the bone pieces were washed in PBS. This was repeated two more times, for a total of three digestions (digestions 1 to 3). Then, bone pieces were incubated with EDTA solution (5 mM EDTA in PBS containing 1% BSA, pH = 7.4) for 25 min. The solution was discarded (digestion 4), and the bone pieces were washed in PBS (digestion 4). Bone pieces were incubated with collagenase solution for 25 min, the solution was discarded, and the bone pieces were washed in PBS (digestion 5). Bone pieces were incubated with EDTA solution for 25 min, the solution was discarded, and the bone pieces were washed in PBS (digestion 6). Bone pieces were incubated with collagenase solution for 25 min, the solution was kept for cell plating, and the bone pieces were washed in PBS (digestion 7). Bone pieces were incubated with EDTA solution for 25 min, the solution was kept for cell plating, and the bone pieces were washed in PBS (digestion 8). Bone pieces were incubated with collagenase solution for 25 min, the solution was kept for cell plating (digestion 9). Digestions 7 to 9 were combined and spun down at 200xg for 5 min. The cell pellet was resuspended in α-MEM culture medium and plated on type-I rat tail collagen coated culture plates. Osteocytes were cultured in α-MEM supplemented with 5% FBS, 5% calf serum, 1mM pyruvate, 100 U/ml penicillin and 0.1 mg/ml of streptomycin. Cells were maintained at 37°C and 5% CO_2 in a humidified incubator up to 7 days.

Animal model

We used eight-week-old C57BL/6 female and male mice. All animal had *ad libitum* access to food (Teklad, 2014: Harlan-Teklad, Indianapolis, IN, USA) and water. Mice

were maintained at 22-24ºC on a 12-hour light/12-hour dark cycle. All procedures were approved by the Ethics Committee for Animal Experimentation of the University of Barcelona and the Generalitat de Catalunya. Osteoblast-specific *Ppargc1a/b*-deficient mice (*Ppargc1a/b*;*Col1a1*-Cre) were generated by crossing heterozygous *Col1a1-Cre* mice (Tg(*Col1a1-cre*)1Kry(21)) with mice carrying loxP sites flanking exons 4 and 5 of the *Ppargc1a* [25] and exons 4 and 5 of *Ppargc1b* alleles [26]. *Ppargc1a/b* f/f;*Col1a1*-Cre (KO) mice were fertile and born in the Mendelian ratio, and they were crossed with *Ppargc1a/b* f/f to obtain experimental (*Ppargc1a/b* f/f;*Col1a1*-Cre) and control (*Ppargc1a/b* f/f) mice.

Retroviral transduction

Retroviral pMSCV-PGC-1α (generated from pcDNA4-PGC-1α from Addgene) and pMSCV-GFP control virus were used for PGC1α overexpression in primary osteoblasts and IDG-SW3 cells. After infection, cells were cultured for five days in osteogenic media. Retroviral pMSCV-puro-Cre-ERT2, pMSCV-puro and pMSCV-GFP virus were used for *Ppargc1*a/b deletion assays in primary osteoblasts from *Ppargc1a/b* f/f mice. Puromycin (5µg/ml) was used for selection of infected cells. 24 hours after selection, tamoxifen was added at 1µM for 48 hours. Cells were then cultured for five more days in osteogenic media.

Alkaline phosphatase and Alizarin Red staining

For alkaline phosphatase, staining solution was added to the cells and incubated at room temperature for 30 minutes in the dark. For Alizarin Red staining, fixed cells were incubated with Alizarin Red staining solution at room temperature in the dark for 45 minutes.

Flow cytometry

Differentiated IDG-SW3, osteoblasts and osteocytes were rinsed twice with PBS. Cells were incubated with 0.25% Trypsin and 0.02% EDTA at 37ºC for 5-10 min, until cells became rounded and started to detach. Cell suspensions were collected and centrifuged at 150g for 5 min. Cell pellets were rinsed three times with PBS and resuspended in PBS containing 1, 5, or 25 mM glucose, 2 mM glutamine and 1 mM pyruvate. Before flow cytometry analysis, cell suspensions were filtered with a 0.70 μm nylon mesh to remove aggregates. Cell viability was assessed with 7-ADD, ensuring that the analyzed population of cells was alive.

Dmp1-GFP expression

Expression of *Dmp1*-GFP in IDG-SW3 was evaluated after 14 days of differentiation by fluoresce microscopy in a Leica DMIRB fluoresce microscope and flow cytometry in a DB FACS Canto II flow cytometer.

Cell proliferation assay

IDG-SW3, osteoblast and osteocyte proliferation was evaluated using BrdU labeling (BD, CA, USA), following the manufacturer's protocol. Briefly, 2×10^4 cells were seeded and cultured for 14- 10 or 7 days. Then, BrdU (10 μM) was added to the medium for 6 hours. Cells were harvested, fixed and permeabilized. The samples were treated with DNase (300 μg/mL in PBS) for 1 hour at 37ºC. BrdU was stained with APC-conjugated anti-BrdU antibody. Cells were analyzed in a DB FACS Canto II flow cytometer.

Cell death detection assay

DNA cleavage was assessed by the TUNEL assay as described by the manufacturer (Roche Molecular Biochemicals). Briefly, IDG-SW3, osteoblast or osteocytes were cultured for 14, 10 or 7 days and then fixed with 4% paraformaldehyde in PBS pH 7.4 at room temperature for 1 h. Cells were permeabilized with 0.1% Triton

X-100 in sodium citrate buffer for 2 min at 4 °C and incubated with TUNEL reaction mixture for 1 h at 37 °C. Total DNA was stained with DAPI (1μg/ml, D9542, Sigma) diluted in PBS for 20 min at room temperature. Coverslip were mounted with ProLong®Gold antifade reagent (P36939, Life Technologies). DNA damage was visualized by fluoresce microscopy in a Nikon E800 microscope. Images were analyzed using ImageJ software.

Fluorescence confocal imaging

IDG-SW3 and primary osteoblasts were cultured in differentiation media for 14 and 10 days, respectively. For Mitocondria visualization, cell cultures were stained with 250nM Mitotracker-Deep-Red (ThermoFisher) for 30 minutes at 37ºC. Then, the cells were examined in a Zeiss LSM 880 laser scanning confocal spectral microscope equipped with an incubation control system (37 °C, 5% CO_2). Images corresponding to single confocal sections were taken using a 63x oil immersion objective lens. Images were analyzed using ImageJ software.

For the staining of actin filaments, cells were fixed in 4% paraformaldehyde in PBS for 15 min at room temperature, washed twice in PBS, permeabilized for 15 min in PBS containing 0.1% Triton X-100, and then blocked in PBS containing 1% BSA for 30 min. To visualize F-actin, cells were incubated with 7.5 units of Alexa Fluor 488 phalloidin (Invitrogen) for 1 hour and washed three times with PBS. DNA was stained with DAPI (1μg/ml, D9542, Sigma). Coverslips were air dried and mounted with ProLong Gold antifade reagent (P36939, Life Technologies). Several z-stack images of 0.4 μm were acquired using Zeiss LSM 880 laser scanning confocal spectral microscope and processed using ZEN software 2010 (Zeiss) to obtain a Maximum Intensity Projection for each Z-stack series.

Gene expression

Total RNA was isolated from mouse calvaria, primary osteoblasts or IDG-SW3 cells using TRIsure reagent (Bioline, London, UK). Purified RNA was reverse-transcribed using the High-Capacity cDNA Reverse Transcription Kit (Applied Biosystems, Foster City, CA, USA). Quantitative PCR was carried out using the ABI Prism 7900 HT Fast Real-Time PCR System and a Taqman 5′-nuclease probe method (Applied Biosystems) with SensiFAST Probe Hi-ROX Mix (Bioline). All transcripts were normalized to TATA binding protein (*Tbp*) expression.

Glucose uptake

The uptake of 2-deoxyglucose was studied in IDGs grown for 14 days in 1, 5, and 25 mM glucose in osteogenic media. Cells were washed four times with pre-warmed PBS, incubated with PBS containing 50Ci/mmol of 2-deoxy-D-[G-^{3}H] glucose and 10µM of cold 2-deoxy-D-glucose for 5 min at 37 ℃. Monolayers were washed 4 times with cold PBS and lysates were obtained in 0.4M NaOH.

Lactate assay

L-lactate was determined using an enzymatic reaction based on the oxidation of L-lactate to pyruvate by lactate dehydrogenase. Samples were diluted by 1:20 with reaction buffer (0.3M hydrazine sulphate, 0.87M Glycine, 2.5 mM NAD$^+$, 0.19M EDTA, pH 9.5). NADH concentration was determined by measuring absorbance at 340 nM using Fluostar Optima BMG Labtech at 0 and 20 minutes after starting reaction.

Intact cell respirometry

Mitochondrial function of intact cells was measured by high-resolution respirometry (Oxygraph-2k, Oroboros Instruments). IDG-SW3 cells were cultured in differentiation media with the indicated glucose concentration for 14days. Cells were trypsined and resuspended again in differentiation media with 1, 5, or 25 mM glucose without FBS. 700,000 cells were added to the experimental chamber. Endogenous routine

respiration was measured with 1, 5, and 25 mM glucose as substrates. Following stabilization of routine respiration, ATP synthesis was inhibited with 1µg/ml of oligomycin to analyze respiratory uncoupling. Next, carbonylcyanide-4-(trifluoromethoxy)-phenyl-hydrazone 1 µM (FCCP) was titrated to achieve maximum flux through the electron transfer system (ETS). Finally, respiration was inhibited by the sequential addition of rotenone (0.1 µM) and antimycin A (2.5 µM). The remaining O_2 flux after inhibition with antimycin A (O_2 flux independent of the electron transfer system) was subtracted to calculate the different respiratory states. Oxygen flux values were expressed relative to protein content determined by the BCA method.

ATP bioluminescence assay

ATP was detected by luciferin-luciferase-ATP reaction. IDGs were lysed in 500µl of boiling water. Extracts were spin at 12000g and 4°C for 5 minutes and 10 µl of supernatant were used for ATP determination. Luciferin-luciferase assay was performed following the manufacturer's recommendations (rLucHS, Biovision).

Western blot assay

Identification of proteins from cell extracts was performed by immunoblotting against pp38, pEIF2α, pS6, LC3, ATF4, SIRT1, pAMPK, pACC, PGC1α, Oxphos, GLUT1 or α-TUBULIN), diluted at 1:1000. Immuno-reactive bands were detected with horseradish-peroxidase-conjugated secondary antibodies and an EZ-ECL kit (Biological Industries, Cromwell, CT, USA).

Chromatin immunoprecipitation assay

ChIP assay was performed as previously described [27]. IDG-SW3 cells were retrovirally-infected with *Ppargc1a* constructs. Cells were cultured for 5 days and fixed in 1% formaldehyde for 10 minutes. ChIP was carried out using 1 µg of anti-PGC-1α

(Abcam) or anti-IgG (Upstate) and purified with 20 μl Magna ChIP Protein A+G Magnetic Beads (Millipore). Purified DNA fragments were analyzed by qPCR with SYBR Green. The primers used for the analysis for *Dmp1*, *Fgf23* and *Sos*t gene promoters are detailed in (Supplementary Table 2).

Determination of mtDNA by qPCR

Two μg of total DNA were used for mitochondrial DNA determination by qPCR. Primers for a mitochondrial DNA gene (*tRNA-Glu*) and a nuclear DNA gene (*Fgf23*) were used. The cycling conditions used were 43 cycles of 30 seconds at 95°C, 30 seconds at 70ºC, and 60 seconds at 72°C.

μCT analysis

Femurs from mice were dissected, cleaned of soft tissue, and fixed in 4% paraformaldehyde (PFA) for 48 hours. High-resolution images from the femur were acquired using a microCT imaging system (Skyscan 1076, Bruker microCT, Kontich, Belgium) in accordance with the recommendations of the American Society of Bone and Mineral Research (ASBMR). Samples were scanned in air at 50 kV and 200 μA with an exposure time of 800 ms, using a 1-mm aluminium filter and an isotropic voxel size of 9 μm. Two-dimensional images were obtained every 1° for 180° rotation and were subsequently reconstructed using NRecon reconstruction software and analyzed with CT-Analyzer (SkyScan). For trabecular measurements, manual VOI was employed, starting at 100 slices from the distal growth plate of the femur and extending to the diaphysis for 150 slices. Cortical measurements were performed by delineating the femur medial cortex for 100 slices around the femoral midshaft. A Gaussian noise filter was applied for the reconstruction, and a global binary threshold was manually established at 20 for trabecular analysis and 100 for cortical analysis.

Histological analysis

For histological preparations, samples were fixed in 4% paraformaldehyde for 48 hours at 4°C, decalcified in 14% EDTA for 4 weeks and paraffin embedded. Samples were cut into 5 µm sections and stained with Hematoxylin/eosin or Masson's trichrome.

Statistical analysis

Statistical analysis was performed using One-way ANOVA or Student's *t* test. Quantitative data are presented as means ± S.E.M. Differences were considered significant at *$p<0.05$, **$p<0.01$ and ***$p<0.001$.